Surface Trajectories of Oil Transport along the Northern Coastline of the Gulf of Mexico

JC Dietrich[a,*], CJ Trahan[a,1], MT Howard[b], JG Fleming[c], RJ Weaver[d,2], S Tanaka[e,3], L Yu[f], RA Luettich Jr[d], CN Dawson[a], JJ Westerink[e], G Wells[b], A Lu[f], K Vega[g], A Kubach[g], KM Dresback[h], RL Kolar[h], C Kaiser[i], RR Twilley[j]

[a]*Institute for Computational Engineering and Sciences, University of Texas at Austin*
[b]*Center for Space Research, University of Texas at Austin*
[c]*Seahorse Coastal Consulting, Morehead City, North Carolina*
[d]*Institute of Marine Sciences, University of North Carolina at Chapel Hill*
[e]*Department of Civil Engineering and Geological Sciences, University of Notre Dame*
[f]*Department of Computer Science, University of North Carolina at Charlotte*
[g]*Texas Advanced Computing Center, University of Texas at Austin*
[h]*School of Civil Engineering and Environmental Science, University of Oklahoma*
[i]*Department of Oceanography and Coastal Sciences, Louisiana State University*
[j]*Vice President for Research, University of Louisiana at Lafayette*

Abstract

After the destruction of the Deepwater Horizon drilling platform during the spring of 2010, the northern Gulf of Mexico was threatened by an oil spill from the Macondo well. Emergency responders were concerned about oil transport in the nearshore, where it threatened immediately the fishing waters and coastline from Louisiana to Florida. In this region, oil movement was influenced by a continental shelf with varying width, the protruding Mis-

*Corresponding Author
Email address: dietrich@ices.utexas.edu (JC Dietrich)
[1]Current affiliation: High Performance Technologies Inc., Vicksburg, Mississippi
[2]Current affiliation: Department of Marine and Environmental Systems, Florida Institute of Technology, Melbourne, Florida
[3]Current affiliation: Earthquake Research Institute, Tokyo, Japan

sissippi River delta, the marshes and bayou of southern Louisiana, and the shallow sounds and barrier islands that protect the coastline. Transport forecasts require physics-based computational models and high-resolution meshes that represent the circulation in deep water, on the continental shelf, and within the complex nearshore environment.

This work applies the coupled SWAN+ADCIRC model on a high-resolution computational mesh to simulate the current velocity field on the continental shelf, nearshore and marsh areas during the time that oil was visible on the surface of the Gulf. The SWAN+ADCIRC simulations account for the influence of tides, riverine discharge, winds and wind-driven waves. A highly-efficient Lagrangian particle transport model is employed to simulate the surface trajectories of the oil. The transport model accounts for dispersion and advection by wind and currents. Transport is evaluated using two week-long sequences of satellite images. During both periods, the SWAN+ADCIRC current fields alone appeared to be more successful moving the oil than when direct wind forcing was included. In addition, hypothetical oil transport is considered during two hurricane scenarios. Had a hurricane significantly impacted the areas, depending on its track, oil would have moved farther into the marshes of southern Louisiana or farther along the shelf toward Texas than actually occurred during the spill.

Keywords:

Deepwater Horizon oil spill, Particle tracking, Nearshore waves and circulation, SWAN, ADCIRC

---

1. Introduction

Surface transport of oil in the open ocean is governed by a multitude of physical and chemical processes (Spaulding, 1988; ASCE, 1996; Reed et al., 1999). Oil is advected by the surface currents associated with tides, riverine discharge, oceanographic currents, meteorological forcing and breaking waves, and by direct wind forcing at the sea surface. Oil disperses and emulsifies, evaporates and decomposes. Each of these processes becomes relatively more or less significant, depending on the properties of the oil, the climatological characteristics of the spill location and the length of time the oil is in the water.

Transport can be particularly complex when oil is released on or near a continental shelf. For example, in the northern Gulf of Mexico, a variety of physical features affect the advection of oil. The continental shelf is relatively wide along the Florida coastline, again near Mississippi and eastern Louisiana, and then again near western Louisiana and Texas. But the shelf narrows near Pensacola, Florida, and also near the "bird's foot" of the Mississippi River delta. The Mississippi River extends to the edge of the shelf, and its outflow affects the local currents. The low-lying topography of southern Louisiana contains networks of marshes and bayous, coastal inlets, and man-made channels that connect the inland water-bodies to the sea. In contrast, the Mississippi-Alabama-Florida coastline is steeper and does not contain the same extent of low-lying marshes, but it features several bays and estuaries that are protected by shallow sounds and barrier islands.

There was significant interest in the transport of oil in this region during 2010. In the spring, the Transocean Deepwater Horizon platform, located

about 66km from the Louisiana coastline, was drilling an exploratory well for British Petroleum in about 1500m of water. During the evening of 20 April, the drilling platform was engulfed by an explosion of methane gas that erupted from the well. The platform burned for more than 24hr before sinking on 22 April. The resulting release from the wellhead has been estimated to have begun at a rate of $9900 m^3 d^{-1}$ and diminished over time to a final rate of $8400 m^3 d^{-1}$ when the well was capped on 15 July 2010 (Robertson and Krauss, 2010; NCBPDWHOSOD, 2011).

The subsurface oil release caused the spill to interact with the marine environment in a manner that was different from that observed in previous surface spills. Near the wellhead, 0.77 million gallons of chemical dispersants were applied to the release, in what was their first large-scale application in deep water (Kujawinski et al., 2011). As a result, the oil in the subsurface plume acquired characteristics that were different than the surface oil, which was treated with an additional 1.4 million gallons of dispersants (Diercks et al., 2011). The plume itself was difficult to observe and quantify, partly because it was a target for biodegradation, which has been shown to be an effective natural remediation for previous spills along shorelines with permeable sediments (Lindstrom et al., 1991; Bragg et al., 1994; Rosenberg et al., 1996). Extensive biodegradation was observed in the deep plume (Camilli et al., 2010; Hazen et al., 2010; Valentine et al., 2010; Kessler, 2011), as well as near the surface (Edwards et al., 2011).

The oil spill posed a serious environmental threat to the northern Gulf coastline from Florida to Texas. Oil was observed within the marshes and along the beaches from Louisiana to Florida, where it was impacted signifi-

cantly by biodegradation before settling to the seafloor (Scholz et al., 1999; Lubchenco et al., 2010; Kostka et al., 2011). There was also concern that it would be carried by the Loop Current to more distant regions. Early predictions showed the potential for oil to make its way to the Atlantic Ocean and the eastern seaboard of the United States (Maltrud et al., 2010).

Another looming concern was the potential that a major storm could impact the northern Gulf during the spill. A landfalling hurricane, such as the storms of 2004 (Ivan), 2005 (Katrina, Rita) or 2008 (Gustav, Ike), would have mixed the oil through the water column and may have pushed it substantially inland. Some portion of this oil would presumably have remained in the low-lying marshes and bayous of the region after the storm waters receded. Ultimately, the 2010 Atlantic hurricane season was relatively uneventful in the Gulf of Mexico, with only Hurricane Alex moving through the southern Gulf while the spill was active. Emergency management officials remained concerned about the possibility of a large storm and its interaction with the oil throughout much of the summer of 2010.

Forecasts of oil movement require well-resolved, physics-based computational models. These models must represent accurately the water velocity and direct wind forcing over the entire domain of interest, from deep water, to the continental shelf, to the marshes, rivers and man-made channels of the complex nearshore environment. There are several existing operational models for oil spill forecasts. The General NOAA Operational Modeling Environment (GNOME, `http://response.restoration.noaa.gov/software/gnome/gnome.html`) is developed and made available by NOAA, and its graphical interface is useful for spills on smaller scales (Beegle-Krause,

1999, 2001). Other operational systems have been applied to the Prestige accident (Castanedo et al., 2006), and along the Norwegian coast (Brostrom et al., 2011). In addition, a team from the University of South Florida developed an ensemble forecast system during the Deepwater Horizon spill (Liu et al., 2011a,b), but with a focus on regional and global scales.

The ADvanced CIRCulation (ADCIRC) model has been employed successfully to coupled wind, wind-wave, tide and riverine flow simulations on unstructured meshes in many geographical regions including the Gulf of Mexico (Mukai et al., 2002; Westerink et al., 2008; Bunya et al., 2010; Dietrich et al., 2010, 2011b). The model has been applied extensively to hurricane forecasts and hindcasts for the development of coastal risk assessments and the design of levee protection systems (Ebersole et al., 2007; FEMA, 2009; USACE, 2009). ADCIRC has been coupled recently to the Simulating WAves Nearshore (SWAN) model, so that both models run on the same unstructured meshes and on the same computational cores (Zijlema, 2010; Dietrich et al., 2011a). The resulting SWAN+ADCIRC model is well-positioned to simulate accurately and efficiently the propagation of wind-waves, tides and storm surge from deep water onto the continental shelf and into the nearshore (Van Cooten et al., 2011; Dietrich et al., 2012).

Recent simulations of oil transport have employed passive tracers (Maltrud et al., 2010; Chang et al., 2011) or have considered the fate and transport of oil movement (Azevedo et al., 2009; Mariano et al., 2011), but on relatively coarse meshes and in deep water. Velocity fields generated by ADCIRC have been applied previously to particle-tracking simulations in the nearshore (Luettich et al., 1998; Churchill et al., 1999; Carr et al., 2005; Oliveira et al.,

2006; Reyns et al., 2006), and herein the velocity field from SWAN+ADCIRC and the imposed wind velocity are used as forcing for the transport of oil as Lagrangian particles. The particle transport algorithm is a Lagrangian solver with an adaptive Runge-Kutta time-integrator. Diffusion is handled through the addition of stochastic fluctuations in the particle velocities. The input wind velocities and computed ADCIRC currents are read into the transport algorithm as the particles evolve. As many as 11 million oil particles can be advected efficiently within an unstructured mesh containing 10 million elements.

Emergency responders employed satellite image assets to map the position and measure the surface extent of the oil spill. Remote sensing analysts of the Satellite Analysis Branch (SAB) within the National Oceanic and Atmospheric Administration (NOAA) National Environmental Satellite, Data, and Information Service (NESDIS) Office of Satellite Data Processing and Distribution performed the manual delineation and data integration leading to NOAA's Experimental Marine Pollution Surveillance Report, the daily source of the surface oil extent map used herein (NOAA, 2010). SAB analysts published daily updates, which were then combined by analysts into a daily composite product. They also provided data for the impact region collected by individual sensors at recurring intervals under daylight and night-time conditions. Initial particle conditions representing the observed distribution of surface oil were generated by reprojecting SAB's vector shapefile data for export to the particle tracking model.

Results from this study indicate that the set of models that have been developed can transport the surface oil layer with a high degree of realism.

When the predicted oil locations are compared against these observations from June-July 2010, the predictions show an overlap of 60 percent or greater, even as much as a week into the simulation. When the observations and predictions are aggregated over longer durations, to account for the variability in the observations, the overlap increases to about 80 percent. This good performance is an indication that the transport can be useful in a forecasting operation.

The set of models has also been applied to hypothetical scenarios where oil spills are transported during hurricane wind forcing. Katrina tracked directly through the region, and its associated winds and currents would have pushed oil far into the marshes, as well as around the Chandeleur Islands and into Lake Pontchartrain. In contrast, although Ike tracked farther westward, its winds in southern Louisiana would have pushed oil around the Mississippi River delta and toward Texas. Based on these simulations, depending on the track of the land-falling hurricane and its associated wind field, oil can be pushed farther into the marshes and inland water bodies of southern Louisiana, or it can be pushed along the continental shelf.

2. Methods

2.1. Wind Forcing

The wave, circulation and particle-tracking models were forced by winds from the North American Mesoscale (NAM) model run by the National Centers for Environmental Prediction (NCEP, `http://www.ncep.noaa.gov/`). NCEP was running operationally the Weather Research and Forecasting Non-Hydrostatic Mesoscale Model (WRF-NMM) as its NAM model at the time of

the event. WRF-NMM uses an Arakawa E-grid and a hybrid pressure-sigma relationship for vertical layer spacing (Janjic et al., 2001; Janjic, 2003).

The WRF-NMM was run at NCEP on a Lambert Conformal grid with 12km horizontal resolution and 60 vertical layers. NCEP ran the model every six hours, producing a nowcast and an 84 hour forecast with output at 3hr temporal resolution. It distributed the output products to the public via the NOAA Operational Model Archive Distribution System (NOMADS, `http://nomads.ncdc.noaa.gov/`).

These data were downloaded in real time and then converted for use in SWAN+ADCIRC. The original data are provided in binary format; the first step in the conversion process was the extraction of atmospheric pressure and wind velocities at mean sea level in ASCII format. The data were then reprojected from Lambert Conformal to geographic coordinates and interpolated onto a set of points that covered the region of interest. The magnitude of the wind velocity was multiplied by 0.893 to recast the winds from a 1min averaging period to a 10min averaging period (Powell and Houston, 1996). The reprojected and interpolated meteorological data were input to the system of models over their entire domain.

2.2. ADCIRC

ADCIRC applies the continuous-Galerkin finite-element method to solve forms of the shallow-water equations for water levels ζ and either the 3D or the 2D, vertically-integrated, momentum equations for water velocity (U, V) (Kolar et al., 1994a,b; Luettich and Westerink, 2004; Dawson et al., 2006; Westerink et al., 2008). The model utilizes unstructured meshes, and thus it allows localized refinement in regions where the solution gradients are largest.

The vertically-integrated forms of the equations are employed herein because it is assumed that the water column is well-mixed, particularly on the mid- to inner-continental shelf, and especially during the hypothetical storm events discussed below. These depth-averaged currents provide a general circulation pattern, which can be augmented for the oil transport forcing through the addition of a percentage of the wind velocities, as described below. However, it should be noted that the lack of variation in the vertical direction is a potential source of error in the transport simulations that follow.

ADCIRC computes water levels via the solution of the Generalized Wave Continuity Equation (GWCE), which is a combined and differentiated form of the continuity and momentum equations:

$$\frac{\partial^2 \zeta}{\partial t^2} + \tau_0 \frac{\partial \zeta}{\partial t} + S_p \frac{\partial \tilde{J}_\lambda}{\partial \lambda} + \frac{\partial \tilde{J}_\phi}{\partial \varphi} - S_p U H \frac{\partial \tau_0}{\partial \lambda} - V H \frac{\partial \tau_0}{\partial \varphi} = 0$$

where:

$$\begin{aligned} \tilde{J}_\lambda = -S_p Q_\lambda \frac{\partial U}{\partial \lambda} - Q_\varphi \frac{\partial U}{\partial \varphi} + f Q_\varphi - \frac{g}{2} S_p \frac{\partial \zeta^2}{\partial \lambda} - g S_p H \frac{\partial}{\partial \lambda} \left[\frac{P_s}{g \rho_0} - \alpha \eta \right] \\ + \frac{\tau_{s\lambda,winds} + \tau_{s\lambda,waves} - \tau_{b\lambda}}{\rho_0} + (M_\lambda - D_\lambda) \\ + U \frac{\partial \zeta}{\partial t} + \tau_0 Q_\lambda - g S_p H \frac{\partial \zeta}{\partial \lambda} \end{aligned}$$

and:

$$\tilde{J}_\varphi = -S_p Q_\lambda \frac{\partial V}{\partial \lambda} - Q_\varphi \frac{\partial V}{\partial \varphi} - f Q_\lambda - \frac{g}{2}\frac{\partial \zeta^2}{\partial \varphi} - gH\frac{\partial}{\partial \varphi}\left[\frac{P_s}{g\rho_0} - \alpha\eta\right] + \frac{\tau_{s\varphi,winds} + \tau_{s\varphi,waves} - \tau_{b\varphi}}{\rho_0} + (M_\varphi - D_\varphi) + V\frac{\partial \zeta}{\partial t} + \tau_0 Q_\varphi - gH\frac{\partial \zeta}{\partial \varphi}$$

and the vertically-averaged currents are obtained from the momentum equations:

$$\frac{\partial U}{\partial t} + S_p U\frac{\partial U}{\partial \lambda} + V\frac{\partial U}{\partial \varphi} - fV = -gS_p\frac{\partial}{\partial \lambda}\left[\zeta + \frac{P_s}{g\rho_0} - \alpha\eta\right] + \frac{\tau_{s\lambda,winds} + \tau_{s\lambda,waves} - \tau_{b\lambda}}{\rho_0 H} + \frac{M_\lambda - D_\lambda}{H}$$

and:

$$\frac{\partial V}{\partial t} + S_p U\frac{\partial V}{\partial \lambda} + V\frac{\partial V}{\partial \varphi} + fU = -g\frac{\partial}{\partial \varphi}\left[\zeta + \frac{P_s}{g\rho_0} - \alpha\eta\right] + \frac{\tau_{s\varphi,winds} + \tau_{s\varphi,waves} - \tau_{b\varphi}}{\rho_0 H} + \frac{M_\varphi - D_\varphi}{H}$$

where $H = \zeta + h$ is total water depth; ζ is the deviation of the water surface from the mean; h is bathymetric depth; $S_p = \cos\varphi_0/\cos\varphi$ is a spherical coordinate conversion factor and φ_0 is a reference latitude; U and V are depth-integrated currents in the λ- and φ-directions, respectively; $Q_\lambda = UH$ and $Q_\varphi = VH$ are fluxes per unit width; f is the Coriolis parameter; g is

gravitational acceleration; P_s is atmospheric pressure at the surface; ρ_0 is the reference density of water; η is the Newtonian equilibrium tidal potential and α is the effective earth elasticity factor; $\tau_{s,winds}$ and $\tau_{s,waves}$ are surface stresses due to winds and waves, respectively; τ_b is bottom stress; M are lateral stress gradients; D are momentum dispersion terms; and τ_0 is a numerical parameter that optimizes the phase propagation properties (Kolar et al., 1994a; Atkinson et al., 2004).

2.3. SWAN

SWAN represents the wave field as a phase-averaged spectrum (Booij et al., 1999), because individual wind waves exist on length- and time-scales that are too small to be resolved when computational models are applied to large domains. The wave action density $N(t, \lambda, \varphi, \sigma, \theta)$ is allowed to evolve in time (t), geographic space (λ, φ) and spectral space (with relative frequencies σ and directions θ), as governed by the action balance equation:

$$\frac{\partial N}{\partial t} + \frac{\partial}{\partial \lambda}[(c_\lambda + U)N] + \cos^{-1}\varphi \frac{\partial}{\partial \varphi}[(c_\varphi + V)N \cos\varphi] + \frac{\partial}{\partial \theta}[c_\theta N] + \frac{\partial}{\partial \sigma}[c_\sigma N] = \frac{S_{tot}}{\sigma}$$

where (c_λ, c_φ) is the group velocity, (U, V) is the ambient current, and c_θ and c_σ are the propagation velocities in the θ- and σ-spaces. The source terms S_{tot} represent wave growth by wind; action lost due to whitecapping, surf breaking and bottom friction; and action exchanged between spectral components due to nonlinear effects in deep and shallow water.

The structured-mesh version of SWAN employs a Gauss-Seidel sweeping algorithm to propagate the wave action density in geographic space, and an

analog of that algorithm was used recently to extend SWAN to run on unstructured meshes (Zijlema, 2010). The coupling of SWAN+ADCIRC allows both models to utilize the same global and local meshes, so that information is passed between models at the mesh vertices, without the need for interpolation between heterogeneous meshes (Dietrich et al., 2011a, 2012). ADCIRC passes water levels and currents to SWAN, while SWAN passes wave radiation stress gradients to ADCIRC. In this study, the wave field is included to capture the nearshore set-up and current forcing provided by the wave radiation stress gradients. In severe events such as hurricanes, the associated set-up can increase water levels by as much as 35 percent in regions near the dissipation zones (Resio and Westerink, 2008; Dietrich et al., 2010).

2.4. SL16 Unstructured Mesh

SWAN+ADCIRC utilizes the Southern Louisiana (SL16) unstructured mesh (Dietrich et al., 2011b, 2012), which offers a high-resolution depiction of the north-central Gulf coastline, including the inland water bodies, marshes and floodplains from Mobile Bay to the Louisiana-Texas border. The mesh provides coverage of the entire Gulf of Mexico, Caribbean Sea, and outward to the Atlantic Ocean (Figures 1-2). For hurricane applications, this wide coverage allows storms to be started within the domain but far from the region of interest. The SL16 mesh contains 5,075,008 vertices and 10,028,691 triangular elements, with the vast majority concentrated along the coastline of the northern Gulf.

Bathymetry was specified via the latest data sets and surveys from NOAA and the USACE, while coastal land-surface topography was specified from LiDAR and land cover databases (Dietrich et al., 2011b). These data were

applied using an averaging at the mesh scale, to avoid irregularities or discontinuities that would arise from a nearest-value interpolation. The continental shelf is represented at a high level of resolution (Figure 3), including the broad and shallow Louisiana-Mississippi shelf, the relatively narrow region near the "bird's foot" of the Mississippi River delta, and the broad Louisiana-Texas shelf to the west of the delta. The marshes of southern Louisiana have topographies of 1-2m relative to NAVD88 (2004.65), while the coastal plains of Mississippi and Alabama rise to elevations of 10-20m. The mesh sizes are 4-6km within the Gulf, no larger than 1km on the continental shelf, and 200m or smaller in the dissipation zone and inland. The mesh sizes vary down to 20-50m in the small-scale channels of southern Louisiana. The SWAN+ADCIRC model, executed on this mesh, has been validated extensively for hurricane applications throughout the region (Dietrich et al., 2011b, 2012).

2.5. Lagrangian Particle Transport

Surface oil advection is assumed to have two primary drivers: water current velocity and winds. Water current velocities are computed and stored by the SWAN+ADCIRC model and thereafter supplied to the particle tracking model. Winds indirectly drive the oil particles due to their contribution to the water currents. Additionally, winds may have a more direct effect on surface oil advection by causing the oil to slip along the water surface. To account for both effects, the total velocity used to advect the oil is computed as the sum of the water velocity $\mathbf{u}_c$ plus a fraction of the wind velocity $\mathbf{u}_w$:

$$\mathbf{u}(\mathbf{x}_p) = F_c \mathbf{u}_c(\mathbf{x}_p) + F_w \mathbf{u}_w(\mathbf{x}_p), \tag{1}$$

where $\mathbf{x}_p = (x_p, y_p)$ are the scattered particle positions and F_c, F_w are multipliers for the currents and winds, respectively. In the absence of currents, F_w is often assumed to be in the range of 0.03-0.035 (Reed et al., 1994). We present three scenarios: (i) oil transport due to currents only ($F_c = 1$ and $F_w = 0$), (ii) oil transport due to currents plus 1 percent of the wind velocity ($F_c = 1$ and $F_w = 0.01$), and (iii) oil transport due to currents plus 3 percent of the wind velocity ($F_c = 1$ and $F_w = 0.03$).

When applying the direct wind forcing, a deflection angle is used typically to account for Coriolis effect. We present results using a 7° deflection angle (Samuels et al., 1982), although the literature supports angles from $3 - 28^\circ$ (Stolzenbach et al., 1977; Audunson, 1980; Reed et al., 1990; Spaulding et al., 1993; Al-Rabeh, 1994). Our experiments with significantly different deflection angles indicated that oil was pushed in unreasonable directions.

Before settling on the three scenarios described above, we considered and ultimately discarded more complex combinations of current and wind forcing mechanisms. A formulation by Youssef (1993) allows the wind multiplier F_w and the deflection angle to vary based on the wind speed and water depth. This formulation was implemented in the tracking algorithm along with an adjustment to account for the ambient currents. However, it was found to push the oil too much in deep water; the predicted oil movement was much stronger to the south and west than was observed. Initial tests with the General NOAA Operational Modeling Environment (GNOME, `http://response.restoration.noaa.gov/software/gnome/gnome.html`) showed similar behavior to the results presented herein, but on a much smaller scale, because its graphical user interface limits the

size of the unstructured mesh and the number of oil particles (Beegle-Krause, 1999, 2001). Therefore our analyses contain a much higher resolution and cover a much larger area.

When an oil slick is dispersed, an expanding cloud of oil droplets is formed and diffused from turbulence, which is parameterized with a random walk in the two horizontal dimensions. This stochastic velocity perturbation is combined with the deterministic current- and wind-driven particle velocities so that:

$$\mathbf{x}_p(t + \Delta t) = \mathbf{x}_p(t) + \mathbf{u}(t)\Delta t + \mathbf{D}, \tag{2}$$

where $\mathbf{D} = (D_x, D_y)$ are the horizontal diffusion perturbations:

$$\mathbf{D} = (2R - 1)\sqrt{\mathbf{c}\mathbf{E}_v \Delta t}, \tag{3}$$

where $0 \leq R \leq 1$ is a random number, $E_{v,x} = E_{v,y} = 10\, m^2\, s^{-1}$ are the turbulent coefficients, and $c_x = c_y = 12$ are scaling coefficients (Proctor et al., 1994).

To locate the particles on the SL16 unstructured mesh, a lattice cell search algorithm was implemented. The finite-element domain is divided into lattice cell sections, and a cell-element list table is constructed. Then the particle location is searched only in elements that are contained within the same cell that contains the particle. The cell address $\mathbf{i} = (i_x, i_y)$ is determined as follows:

$$\mathbf{i} = int[(\mathbf{x}_p - \mathbf{x}_0)/\Delta \mathbf{x}], \tag{4}$$

where $\mathbf{x}_0 = (x_0, y_0)$ are the origin of the lattice cell, and $\Delta\mathbf{x} = (\Delta x, \Delta y)$ are the cell widths for the x- and y-coordinates. Once the finite element containing the particle is located, the velocity field is interpolated linearly to the location of the particle itself.

The particle transport algorithm is parallelized via a hybrid MPI-OpenMP implementation. The total number of particles is divided over the total number of MPI nodes, and each MPI node tracks the movement of its subset of particles in the entire finite element domain. On each MPI node, information is stored about the global mesh and velocity field, and the particle transport procedure is parallelized by OpenMP threads on the computational cores within that MPI node. Thus, the cores within an MPI node share the global mesh and velocity field, but each core computes the advection of an individual parcel of oil particles.

The parallelized transport code is highly efficient. The code was run on the Ranger high-performance computing system at the Texas Advanced Computing Center at the University of Texas at Austin (TACC, `http://www.tacc.utexas.edu`), typically on 16 Sun Blade x6420 nodes, each with 4 quad-core AMD Opteron 8356 CPUs, for a total of 256 computational cores. The hybrid MPI-OpenMP parallelization allows the particle transport portion of the code to scale linearly, especially when binary file input/output is implemented via NetCDF. On those 256 computational cores, the resulting code can transport 11 million particles on an unstructured mesh with 10 million triangular elements in about 5.5min per day of simulation.

3. Tracking of Oil during the 2010 Hurricane Season

3.1. Forecast Tracking

During the course of the oil spill in 2010, SWAN+ADCIRC and the particle tracking model were run as a quasi-operational forecasting system. This system required the development of an automated approach to running these models on a high-performance computing (HPC) platform. Every time a new meteorological forecast is available (typically every 6hr), the latest meteorological data must be downloaded, input files constructed, the HPC jobs formulated and submitted, and results post-processed. If there are network or other outages, the automated system must recover gracefully and continue to produce guidance. Also, because the need for such an automated system is event-driven, it should be geographically agnostic, portable to different HPC platforms and as flexible as possible.

In order to meet these requirements for the Deepwater Horizon event, the ADCIRC Surge/Spill Guidance System (ASGS) was deployed (Fleming et al., 2008). This software system was designed to provide resilient, portable automation for quasi-operational ADCIRC forecasts on HPC architectures, and was originally created for use in tropical cyclone events. For tropical cyclones, the ASGS downloads the text of each Forecast/Advisory from the National Hurricane Center (NHC) as soon as it is posted and extracts the information needed as input for one of the tropical cyclone vortex meteorological models within ADCIRC. For the present application, the ASGS was modified to access and process NCEP NAM gridded meteorological files for input to SWAN+ADCIRC and the particle tracking model.

The ASGS also has the capability to post-process the simulation results, which was attractive due to the need to include visualization of the particle tracking. The real-time capabilities afforded by the ASGS made it possible to provide daily forecast guidance on the likely path and coverage of oil in the nearshore from late May through July.

Hindcast simulations for two timeframes during June-July 2010 are used to evaluate the system performance, as discussed below. Wind fields were constructed by stringing together the initial conditions (which included the assimilation of meteorological observations) from consecutive NCEP NAM runs, thereby generating a wind snapshot every 6hr for the duration of the hindcast simulation.

3.2. Satellite Imagery

Emergency responders employed satellite and aerial image assets to map the position and measure the extent of the oil spill. Aerial imagery was used tactically near the wellhead and in some places where oil washed ashore, but aerial data were not collected for the entire area or at regular intervals. In contrast, satellite images were collected regularly from late April through August 2010. These images were used to determine the extent and long-range trajectory of the surface oil.

NOAA serves as the lead agency for satellite sensor tasking during oil spill response. During the Deepwater Horizon event, analysts requested data collection using multispectral optical and synthetic aperture radar (SAR) assets. Optical sensors collect passively the visible and infrared radiation reflected or emitted from the Earth's surface. SAR sensors transmit actively the microwave signals and receive the resulting reflections. SAR assets can

collect useful information regardless of sun illumination and cloud cover, in most cases. A suite of sensors provided information nearly every day and night during the period spanning 22 April to 12 August 2010. Table 2 lists the satellite sensors that SAB analysts used to generate NOAA's surface oil product.

Spaceborne SAR sensors are the preferred data source for sea surface oil slick detection because they offer relatively low data cost in comparison to aerial platforms, provide effective day and night cover, have cloud penetration capabilities, and deliver wide area coverage (Brekke and Solbert, 2005). Coverage and spatial resolution for SAR products depends on the requested sensor mode (Table 2). In most cases, modes resulting in moderate resolution (30-100m) data were preferred because they offer the widest possible coverage of the northern Gulf of Mexico without sacrificing detail. Temporal collection windows are predetermined by satellite orbit characteristics. Prime collection times were 0400 and 1600 UTC for Envisat ASAR and ALOS PALSAR, and 0000 and 1200 UTC for the Radarsat and Cosmo SkyMed satellites.

When SAR collections were not available, optical sensor data were analyzed instead. MODIS was the primary sensor used. MODIS was the primary sensor used. MODIS instruments are onboard two NASA missions, Terra and Aqua, which pass over the region at 1500-1600 UTC and at 1800-1900 UTC. Analysts prefer to use cloud-free images with sun glint reflected from the oil slick for easier delineation (Adamo et al., 2009). Oil slick patterns become less obvious outside the sun glint area.

SAB remote sensing analysts used a consistent interpretation methodology and similar data sources, including ancillary data, while delineating oil

slick extent, but there are acknowledged limitations to the resulting product, which remains experimental. The following limitations are noted in the Satellite Derived Surface Oil Analysis Program overview: satellite image coverage may not completely cover the northern Gulf of Mexico each day; cloud cover and data gaps may obscure spill extent in optical data; increased convection such as local thunderstorms may increase wave activity, obscuring oil spill indications; and low winds can create calm water patterns similar to the dampened and darkened surface oil features (NOAA, 2010). In addition, natural oil seeps and biogenic slicks can be confused with surface oil (Alpers and Espedal, 2004).

Oil slick delineation can be particularly challenging in the nearshore environment. The experimental products included commentary indicating possible false positives and delineation confidence level. Certain sensors were available less frequently for tasking. An additional challenge is the need to task an area for collection 1-2 days in advance, which requires both weather and slick transport forecasting. The northern Gulf from eastern Louisiana to the west Florida coast was targeted frequently. Far fewer data frames were collected in the western Gulf.

Initial particle conditions representing the observed distribution of surface oil were generated by reprojecting SAB's vector shapefile data into geographic coordinates and converting them into raster grid cells with uniform spacing. Prior to raster conversion, oil extent polygons were subdivided and attributed with reference to source areas within 6km of the coast, on the continental shelf in waters less than 100m deep, and in waters deeper than 100m (Figure 4). The spacing of cells was set at 50m. Raster data were converted to vector

points, geographic coordinates determined for each point, and coordinates with initial location attributes written to an ASCII format file for export to the particle tracking code. During the spill, a new initial condition for the surface oil location was generated every 24hr and used in the tracking model for the daily forecast guidance. Previous tracking results were ignored in each new forecast. These forecasts had durations of 84hr, corresponding to the length of the wind forecasts provided by NCEP, as described above.

To evaluate the models' performance, two timeframes were selected for analysis in the following sections, and wind fields were created for these timeframes by combining the nowcast winds provided by NCEP throughout the event, as noted above. The first analysis period, during mid-June, corresponded to a time of fair weather conditions, good satellite delineation of the surface oil and the occurrence of oil contamination along the beaches of Mississippi, Alabama and Florida. A total of 26 images were considered for the analysis (Table 3). Initial particle conditions were generated with a uniform spacing of 50m, resulting in a field of 11.5 million particles for this analysis period.

The second analysis period, from late June to early July, includes the passage in the southern Gulf of Mexico of Alex, which was the only 2010 Atlantic hurricane to affect the oil spill region. The initial state of the central Gulf was collected late in the evening on 28 June by two twin sensors, Cosmo SkyMed 2 and 3. The easternmost edge of the oil extent was not in the field of view. A total of 23 individual scenes collected between 29 June and 5 July were considered for use in the model evaluation (Table 4). Initial particle conditions were generated with a uniform spacing of 10m, resulting

in a field of 10.7 million particles for this analysis period. Although the Alex scenario provided the opportunity to track movement under stronger meteorological forcing, those same conditions created increased uncertainty in the delineated products. Also, coverage in the western Gulf was less than optimal. Figures 5-6 summarize the available satellite imagery during these two analysis periods and highlight the regions of uncertainty. Taken together, these periods are a good test of the capability of our system of models to transport oil at the sea surface on the continental shelf and within the nearshore.

3.3. Model Evaluation during 13-23 June 2010

3.3.1. Winds and Circulation

Wind speeds and directions were measured throughout the region (Figure 7) at stations operated by the National Oceanic and Atmospheric Administration (NOAA, `http://tidesandcurrents.noaa.gov/`), as well as at platforms operated by the National Data Buoy Center (NDBC, `http://www.ndbc.noaa.gov/`). The NCEP NAM wind velocities used as input to our models are compared with these data in Figure 8. The first two stations are coastal and the wind speeds show a strong diurnal signal that presumably represents the sea breeze associated with typical summertime, fair weather conditions. While the signal is present in the NAM winds, the sea breeze is a relatively localized phenomenon at the land-water margin and therefore it is not surprising that it is significantly underestimated by the 12km resolution NAM. The NAM model does a much better job of representing the observed wind velocity at the other stations, and particularly at NDBC buoys 42012 and 42020, which are in the midst of our modeling area. During most of the

simulation period the winds blow from the west, although they strengthen and reverse direction to easterly during the final three days.

Comparing the measured and predicted water levels at the NOAA stations (Figure 9), note the good matches in both phasing and amplitude of the diurnal tides. The lone exception is during the neap tide on 18 June; the observations indicate an additional high water that ADCIRC does not capture.

Predicted ADCIRC currents are compared with observed time series of near surface currents at five nearshore NOAA stations along the Mississippi Sound (Figure 10). These measurements are taken near the sea surface. The observed and modeled currents are dominated by the diurnal tidal signal. At each location, the modeled currents capture the direction well and at three sites the velocity magnitude is also captured reasonably well. The most significant outliers are Mobile Bay Buoy M and Pascagoula Harbor LB 10, where the current velocity magnitudes are substantially below those observed. The Pascagoula Harbor LB 10 site is quite close to the Pascagoula LB 17 site, which shows much better agreement with the observations. It is likely that disagreements at specific current meter locations are due to disagreement in the bathymetry between the model grid and the actual terrain. It is noted that errors in the computed currents are a potential source of error in the transport simulations that follow.

3.3.2. Oil Extents in the Northern Gulf

The particle-tracking code was employed as a post-processing step to simulate the surface trajectories of the oil during this time period. Spatial comparisons between the predicted oil locations and selected satellite imagery

are shown for the cases of current velocity forcing only ($F_c = 1$ and $F_w = 0$, in Figure 11), current velocities and 1-percent of the wind velocities ($F_c = 1$ and $F_w = 0.01$, in Figure 12), and current velocities and 3-percent of the wind velocities ($F_c = 1$ and $F_w = 0.03$, in Figure 13). The observations from the satellite imagery are shown in solid blue, while the predicted oil locations are shown with red hatching that varies from light (for particles that started initially in deep water) to dark (for particles that started initially on the shelf). As discussed in further detail below, the scenarios that included direct wind forcing tended to push too much oil onto the Louisiana-Texas continental shelf and spread too much oil into deep water as compared to the satellite imagery. Thus, most of the discussion herein will focus on the results with currents-only forcing.

The oil is conditioned initially (Figure 11a) to be located mostly in regions offshore of Louisiana and the northern Gulf coastline. The exception is the stretch of coastline between the Mobile and Pensacola Bays, where oil is seen to have made contact with the beach. This observation is confirmed by news reports that oil was first observed in this region in early June (National Park Service, 2010), before the conditions shown in this sub-figure.

The currents moved generally eastward during the first 6-7 days of this time period, and this movement is captured both by the observed and predicted oil extents (Figures 11b-d). However, the observations show oil reaching farther east and closer to Florida. This mismatch between the observations and predictions is caused by the limited eastward extent of the initial conditions; note the clearly-defined eastern edge of the initial conditions near Pensacola Bay (Figure 11a). It is likely that the oil extended farther east

than was observed by the satellite at the beginning of this simulation, and this limitation prevents the predictions from matching the eastern extent of the leading edge of the oil spill. The speed of the eastward movement is matched well by the predictions, however. Note that, when the wind velocities are included as forcing to the particle tracking model (Figures 12b-d and 13b-d), the predictions move faster toward the east and match better to the observed leading edge of the oil.

With respect to smaller features, the evaluation is limited to instances when they are observed by the satellite imagery. Where oil was observed along the Alabama and Florida coastlines, it is matched well by the predicted particle movement. Note how the oil has spread eastward in less than two days along the Florida coastline past Pensacola Bay (Figure 11b). Most of that oil is missing from the observations about 2-4 days later (Figures 11c-d), with only patches along the Alabama coastline and much farther east, because of limitations in the satellite imagery.

Some features are present in only a small number of satellite images. For example, the initial conditions (Figure 11a) show no oil to the west of the Mississippi River delta, an area for which satellite observations were not tasked during that time, and that absence is repeated in the majority of the following observations. However, in selected observations like Figure 11e, small patches of oil are observed in Terrebonne Bay. These observations are supported by news accounts of oil within Terrebonne Bay as early as May (DeSantis, 2010; Hatcher, 2010).

In the final 2-3 days of this time period, the winds and currents changed to move westward, and thus oil was pushed onto the Louisiana-Mississippi

continental shelf and threatened the Chandeleur and Mississippi Sound Islands (Figure 11f). Note the edge of the oil spill extents that is just east of the Chandeleur Islands and south of the Mississippi Sound Islands; it is beginning to move northward in both the observations and predictions. Also, for the first time, a small sliver of oil is observed just outside the Chandeleur Islands, and its location is matched well by the predictions. This movement continues later in the simulation, as the oil propagates much closer to the sounds and to Mobile Bay. Note that the predictions with wind velocity forcing deteriorate at this late stage of the period. In Figures 12e-f and 13e-f, there is considerable movement of the predictions to the south and west that is not supported by the satellite imagery.

It is interesting to examine the behavior of the predicted particle movement through time. In Figure 14, the particle locations are sampled and connected across different time snaps to show the trajectories moving from orange to red. The trajectories show a general movement of the oil spill to the north and east. When only the currents are applied as forcing (Figure 14a), the particle motion is limited mostly to the continental shelf, with the particles nearly stationary in deep water. This behavior is supported generally by the observations in Figure 11. When the winds are also included as forcing (Figure 14b-c), the oil particles move too much in deep water, especially to the south and west.

3.3.3. Computed Overlap

To quantify the performance of our oil tracking, surface areas were computed for the observed oil and the overlapping particles. However, there is too much variability in the imagery to allow for a meaningful comparison

of observations and predictions at the individual time snaps, so this process requires some level of aggregation of both the imagery and the predicted particle locations. We present results from two methods of aggregation. The first comparison utilized a relatively small aggregation window for the satellite images only, while the second comparison utilized longer windows for aggregation of both the satellite images and the tracking results.

This period features 26 satellite images for comparison (Table 3), but seven images were discarded due to limited coverage. Another five pairs of images were combined because each pair contained non-overlapping information within an aggregation period of 3hr. Thus, the comparisons were performed at a total of 14 time snaps.

Examining first the performance everywhere, it is important to note the variability in the observed oil spill extents (Figure 15a). The initial conditions cover almost 29,000km^2, but the observed extents range from about 16,600-31,800km^2 during this analysis period. This variability is reflected in the predicted overlapped areas, which begin at the same 29,000km^2 and range downward to 8,000km^2. When the areas are normalized to the observations (Figure 15b), the performance can be quantified.

The wind forcing in deep water has the effect of spreading the particles by too much, relative to the observations. In Figures 15a-b, the overlap percentages decrease significantly when the forcing includes 1-percent (dashed purple lines) or 3-percent (dashed green lines) of the wind velocities. The best response is achieved with only the currents as forcing (dashed red lines). For that case, over the first 3-4 days of the simulation, the overlapped percentage falls to about 65-75 percent, but then it remains relatively constant

for the next 4-5 days. When the winds change direction on 20 June, the overlap deteriorates to about 50 percent.

When the analysis is limited to water depths less than 100m (Figures 15c-d), the performance is very similar. The total areas are much smaller, with the observations starting at 9,600km^2 and ranging from 4,600km^2 to 12,000km^2. But the amount of overlap is roughly the same, with about 50-60 percent after a week of simulation.

To compensate for the variability in the satellite imagery, the aggregation was also performed within a larger time duration for both the satellite images and the predicted particle locations. For each image in the time series, an aggregated probability image is generated via the composition of the nearest neighbor images. The probability P for the current aggregated image and the value for every pixel is calculated by:

$$P = \frac{1}{N} \sum_{i=1}^{N} w_i P_i$$

where N is the number of images used in the aggregation, w_i is a Gaussian weight, and P_i is probability value for each pixel. The Gaussian weight is computed based on the distance from the current time to the time of the neighbor image. The aggregation considers the neighbor images within a 24hr window.

After the satellite images are aggregated, thresholds are established, and the images are normalized to $[0, 1]$. Probabilities are capped at an upper limit of unity. If the probability is less than unity, then a log function is applied to generate smooth edges (Figures 16a,c). The predicted particle locations are aggregated in the same manner, using an identical window in

time (Figures 16b,d). Then, at each time snap, a comparison is made between the aggregated imagery and the aggregated predictions.

The aggregation has the effect of smoothing the observed surface areas (Figures 17a,c). The aggregated observations begin at about 20,000km^2 and reach a maximum of about 48,000km^2. The predictions show a relatively constant overlap of about 40,000km^2. When these areas are normalized (Figure 17b), it becomes evident that the predicted particle locations are showing a relatively constant overlap of 80 percent or larger. This overlap percentage drops slightly when the analysis is performed only on the continental shelf (Figure 17d), to about 70-80 percent. It is interesting that the overlap results are slightly better when the winds are included as forcing to the particle movement. This improvement is due mostly to the lateral spreading caused by the winds; note the increases in the total surface areas (solid purple and green lines in Figures 17a,c) when the winds are included.

3.4. Model Evaluation during 29 June through 4 July 2010

Alex was the first named storm of the 2010 hurricane season. It strengthened as it moved over the Caribbean Sea, and it made landfall as a tropical storm in Belize on 27 June. It retained most of its intensity as it moved over the Yucatan Peninsula and emerged into the southern Gulf of Mexico, where it strengthened further into a Category 2 hurricane before making landfall again in northern Mexico on 1 July (Pasch, 2010).

The second timeframe selected for evaluation of the oil spill transport was during the movement of Alex over the southern Gulf of Mexico and after its landfall, specifically 29 June through 4 July 2010. During this timeframe, the storm never threatened directly the oil spill, but it did create large

waves that propagated northward, and the local winds were blowing generally alongshore. However, although the hurricane produced a relatively more interesting environment of winds, waves and circulation, its far-field cloud coverage and increased wave action hindered the collection of useful satellite sensor image data, thus making difficult the evaluation.

3.4.1. Winds and Circulation

The wind input and predicted ADCIRC water levels and currents were evaluated at the same NOAA stations and NDBC platforms shown in Figure 7. The storm dominated the wind field as far away as the northern Gulf coastline (Figure 18), where the wind speeds vary upward to 4-6 m s^{-1} and as much as 8-10 m s^{-1} during 29 June to 1 July, as the storm reached its peak intensity and made landfall in Mexico. The wind directions in Figure 18 show little variability throughout most of the time period, with most stations and platforms having recorded winds with a relatively constant direction between easterly (90°) and southerly (180°). These winds pushed water and oil onto the Louisiana-Mississippi continental shelf and toward the marshes of southern Louisiana.

The water levels again show a strong diurnal tidal signal although irregularities associated with the winds are also evident (Figure 19). Although the hurricane produced a storm surge of 1.5m along the southern Texas coastline and probably larger in Mexico near landfall (Pasch, 2010), the water levels in this northern Gulf region are generally smaller than 1m. ADCIRC agrees generally with the observations.

As occurred during the earlier time period, the observed current directions are generally well-reproduced by ADCIRC (Figure 20). The current speeds

are larger than before, especially during the early part of the time period and outside Pascagoula, MS, where they range upward to 1 m s^{-1}. ADCIRC captures the current speeds reasonably well at most locations, including the deep-water NDBC platforms. The exception is NOAA station mb0101, where ADCIRC reproduces the direction but not the speed. A similar behavior occurred during the earlier time period and probably represents disagreement between the local model bathymetry and the actual terrain.

3.4.2. Oil Extents in the Northern Gulf

The surface oil advection is particularly sensitive to the wind velocities during this timeframe, because their relative strength and onshore direction can push oil too far toward the marshes of southeastern Louisiana (Figures 21-23). When 1 percent of the winds are included as forcing to the particle tracking model, the oil approaches the edges of the Caernarvon and Biloxi marshes to the east of New Orleans, and the southern marshes near the Terrebonne and Timbalier bays. This movement is exaggerated along the edges of all of these marshes when 3 percent of the winds are included. The satellite observations show some oil approaching the edges of the eastern marshes and progressing along the southern Louisiana coastline, but not as much oil as is blown to those locations when the wind velocities are included as forcing to the particle transport model. Thus the spatial descriptions focus on the predicted oil advection with forcing from currents only, although quantitative comparisons with satellite-derived oil coverage are presented for all three scenarios.

In the initial conditions (Figure 21a), oil has moved toward the north and east in the six days since the end of the previous evaluation period. It is now

observed mostly on the continental shelf, and some oil is observed behind the Chandeleur Islands. In addition, a significant amount of oil has pushed around the delta and is now threatening Grand Isle and the Barataria and Terrebonne Bays. These initial conditions do not identify oil eastward of Mobile Bay, but oil is present in this region in subsequent imagery (Figures 21b,e). Because of the generally-westward winds and currents during this time period, it is unreasonable to expect the oil particles from the initial conditions to move eastward to the new observation locations, and thus the evaluation cannot be performed in this region.

About 36hr into the simulation, oil has moved to the Mississippi coastline and threatens Bay St Louis, and it continues to move westward toward Lake Borgne (Figure 21c). A few days later (Figures 21d-e), the predicted oil progresses into Lake Borgne, and this movement is supported by the observations. The oil also moves through the Chandeleur Sound and toward the Caernarvon Marsh (Figures 21d-f), and thus threatens the southeast edge of metropolitan New Orleans.

Pockets of oil within the Barataria and Terrebonne Bays are present in the initial conditions (Figure 21a), and they are evident in the subsequent observations (Figures 21c-d). In Terrebonne Bay, the observed oil is matched well at times 36hr and 48hr into the simulation. Note that the oil advects mostly along the shelf and toward the west, and does not interact with or move into the bays and marshes of southern Louisiana. In fact, significant amounts of oil are pushed westward along the Louisiana-Texas continental shelf. Slivers of observed oil are present almost as far west as Calcasieu Lake in the only satellite image (Figure 21f) that observed oil in this region. After

6 days of simulation, the predictions match well to this sliver of westward movement, as the winds drove currents around the delta and along the coastline. This westward movement was part of a larger trend during this time period, as the winds and currents pushed oil north and west.

In Figure 24, the particle movement is shown with trajectories transitioning from orange to red. When only the currents are used as forcing (Figure 24a), there is a clear delineation at the continental shelf break, as the majority of the action is limited to shallow water. Particles move around the bird's foot of the Mississippi River delta, as the yellow and orange trajectories are strong in that region. Some particles are pushed to the northeast, onto the Louisiana-Mississippi shelf, and toward the barrier islands and the coastlines of Mississippi and Alabama. Other particles are pushed to the west, along the Louisiana coastline, and a few tracelines extend as far west as Vermilion Bay. The wind forcing exaggerates all of this behavior (Figures 24b-c), and it also pushes too much oil into the marshes of southern Louisiana.

3.4.3. Computed Overlap

This analysis period has a total of 23 satellite images that describe the observed oil spill extents (Table 4), but 10 of those images were discarded because they had insufficient coverage (sometimes as small as 90km^2 of observed oil). Another three pairs of images were consolidated because they offered non-overlapping coverage and were separated in time by no more than 20min. The resulting 10 images were then processed further, as observed oil was discarded if it was located eastward of Mobile Bay, because the initial conditions did not allow for evaluation in that region.

Even after this consolidation and processing, there is significant variability in the observed surface area in Figure 25a. The initial conditions cover 9,800km^2, but then the subsequent images offer coverage that ranges from 2,100km^2 to 13,000km^2. The surface area of overlap from the predicted particle locations shows some of this variability, as it drops immediately to about 2,000km^2, but it remains relatively constant throughout the simulation. When the surface areas are normalized (Figure 25b), it becomes clear that the performance degrades slowly over this time period.

The scenarios including wind forcing show less overlap between the predicted oil movement and the observations, as the results with 1-percent winds (dashed purple lines) and with 3-percent winds (dashed green lines) are generally worse. For the case with currents only, after about 36hr, the predicted particle locations show an overlap of about 30 percent of the observed spill extent, and it remains constant for the remainder of the simulation. These overlap statistics reflect the variability in the satellite imagery, as well as the complexity of the winds, waves and circulation during Alex.

When the analysis is performed only on the shelf (Figures 25c-d), the initial surface area is decreased to 7,800km^2, and it ranges from 1,000km^2 to 8,200km^2 over the simulation. However, the overlap between the observations and predictions is very similar, with a relatively constant overlap of 30-40 percent. These results indicate that the wind contribution to the forcing of the oil advection is beneficial in the nearshore, at least with respect to the limited satellite observations.

To account for the variability in the observations, an aggregation was also performed over a longer duration of 24hr, using the technique described

above, and discarding any observed oil to the east of Mobile Bay (Figure 26). The aggregation over the longer time period has the effect of increasing the spatial extents of both observations and predictions. In the images near the end of the analysis period, the aggregation pulls together the sparse observations of oil along the Louisiana-Texas continental shelf into one image (Figures 26c), and this westward movement is matched well by the predictions (Figures 26d).

Once the surface areas have been aggregated around each time snap, the comparison of overlap can be conducted. There is much less variability in the surface areas (Figure 27a), and they show a similar increase during the time period, when there are more available time snaps for the aggregation. The aggregated observed spill extent starts at about 5,700km^2 and ranges upward to 17,500^2, while the aggregated overlapping areas range from about 18,000km^2 to 35,000km^2. The trend in the overlapping areas is similar for all of the wind contributions, with a general decrease in the overlap during the time period. When only the currents are included in the forcing of the particle movement (dashed red line in Figure 27b), the aggregated overlap decreases to about 80-85 percent after 5 days of simulation. Similar behavior is observed on the continental shelf (Figures 27c-d), where the predictions show an overlap of 80-90 percent of the observed spill area.

4. Hypothetical Oil Transport during Hurricane Scenarios

Using the lessons learned and the technology described above, we applied the models to hypothetical oil transport during Katrina and Ike. These storms impacted the northern Gulf in different ways, and they show the

effect of the local wind environment on surface currents and oil transport. For both storms, the oil particles are transported using forcing from the current velocities, but no direct forcing from the winds.

4.1. Katrina (2005)

Katrina was an especially large and devastating storm. It reached Category 5 on the Saffir-Simpson wind scale while in the deeper Gulf, it made landfall as a strong Category 3 storm along the Mississippi River, and it tracked closely to New Orleans as it moved northward. The storm pushed surge into Lake Pontchartrain that caused levee failures and flooding of the city, and it created surge along the Mississippi coastline that was the largest measured in the United States (Ebersole et al., 2007; Bunya et al., 2010; Dietrich et al., 2010).

SWAN+ADCIRC hindcasts of Katrina have been published previously (Dietrich et al., 2011a, 2012). Herein, particles are included to represent the hypothetical transport of oil as the storm moves through the system. The initial conditions (Figure 28a) are taken from the Alex analysis period described above, namely 2010/06/29/0044UTC. They show oil on the continental shelf, pushing against the barrier islands of the Mississippi and Chandeleur Sounds, wrapping around the Mississippi River delta, and stretching along the Louisiana coastline toward Texas. During the Alex timeframe, the oil spill spread over the continental shelf and approached the edges of the marshes and bays in the region, but it did not penetrate.

As Katrina approached the region, the storm moved due northward, and its counter-clockwise rotation allowed strong winds to push waves and surge onto the Louisiana-Mississippi continental shelf for several hours before its

initial landfall along the Mississippi River delta. These winds pushed early surge over the Caernarvon Marsh and into Lake Borgne. In the four hours leading to the initial landfall (Figures 28c-d), the surge would have carried oil to the Mississippi coastline and into southeastern Louisiana. The predictions show that oil has pushed into Lake Borgne and threatens to move into Lake Pontchartrain, and it has pushed over the Chandeleur Sound to the edge of the Caernarvon Marsh. Furthermore, the strong currents around the delta would have pushed a large amount of oil to the southeast and onto the Louisiana-Texas shelf.

In the few hours after its initial landfall, Katrina tracked through the system as a strong storm and made another landfall along the Mississippi coastline (Figures 28e). As the winds shifted to move northerly or even westerly in some regions, the surge slowed its inundation. The city of New Orleans would have been threatened by oil moving into the eastern edge of Lake Pontchartrain, as well as oil moving over the Caernarvon Marsh. Because of the storm's track, there was minimal flooding of the marshes to the west of the river, and thus there would have been minimal oil penetration in these regions. Instead, the spill in this region would have remained offshore, and it would have moved slowly off of the Louisiana-Texas shelf.

By 13hr after the initial landfall (Figure 28f), the surge had reached its maximum inundation and was beginning to recede. The oil spill would have also reached maximum inundation of southern Louisiana. Most of the region east of the river would have been covered with oil that had been pushed past the barrier islands. The Caernarvon and Biloxi marshes would have been inundated fully, and the eastern half of Lake Pontchartrain would experi-

ence a significant presence of oil. The currents were much slower during the post-storm recession and thus a large portion of the oil may have remained attached to any substrate or sediments that it contacted as the waters receded. Katrina would have pushed oil into southern Louisiana, where it may have remained long after the storm waters departed.

4.2. Ike (2008)

Ike moved farther westward and made landfall near Galveston, Texas. Its large size caused its tropical-storm-strength winds to extend into Louisiana as it moved through the central Gulf. These winds pushed surge onto the Louisiana-Mississippi continental shelf and into the Caernarvon Marsh, but they also pushed currents around the Mississippi River delta and onto the Louisiana-Texas continental shelf.

Hindcasts of Ike using SWAN+ADCIRC have been published previously (Kennedy et al., 2011; Dietrich et al., 2012; Hope et al., 2011). Again, we include particles to represent the hypothetical transport of the oil as the storm moves through the system. As before, the initial conditions (Figure 29a) are the same as for the evaluation during Alex, namely 2010/06/29/0044UTC. However, although the oil begins in the same location, it responds differently to the forcing of Ike.

The eye of the hurricane was always more than 100km from New Orleans, but its large size caused its winds to impact southern Louisiana and the Louisiana-Mississippi continental shelf. About 31hr before the storm made its landfall in Texas, it was centered due south of the Mississippi River delta (Figures 29b). The winds in the north-central Gulf are blowing easterly, and they are pushing currents and oil into the Chandeleur Sound and

Lake Borgne. Over the next day (Figures 29c-d), the winds shift to blow southeasterly, and currents and oil are pushed into the Caernarvon Marsh and Lake Pontchartrain, similar to the behavior during Katrina.

However, because Ike tracked farther toward Texas, its winds do not blow offshore to the west of the Mississippi River, as they did during Katrina. Instead, the winds blow easterly and southeasterly in this region, pushing currents and oil around the delta and along the Louisiana-Texas continental shelf. Most of this movement occurs in the days before landfall (Figures 29b-d) as Ike tracked through the Gulf. By its landfall in Texas (Figure 29e), most of the oil has flowed around the delta. It is important to note that the extensive inundation of the marshes along south-central Louisiana, starting at Vermilion Bay and moving westward. The strong currents and surge on the shelf have pushed inland, and oil would have moved into the marshes, far from the spill location. This inundation is still present at 12hr after landfall (Figure 29f). The recession process was slow from these friction-dominated marshes, and thus a large portion of the oil may have remained attached to any substrate or sediments that it contacted as the waters receded. A storm like Ike, although it tracked offshore from the spill, would have pushed oil into the marshes of southern Louisiana and along the continental shelf toward Texas.

5. Conclusions and Future Work

During the spring and summer of 2010, the northern Gulf coastline was threatened by an oil spill that resulted from the explosion of the Deepwater Horizon drilling platform. Oil was released offshore of the Mississippi

River delta, and it moved onto the Louisiana-Mississippi continental shelf, where it interacted with the shoreline from Louisiana to Florida. Emergency managers required detailed forecasts of the oil transport, and were concerned particularly about the possible movement of a landfalling hurricane through the region.

Transport forecasts require physics-based computational models that represent the important processes that contribute to oil movement in deep water, on the continental shelf, and within the complex nearshore environment. The integrally-coupled, SWAN+ADCIRC model was employed herein to simulate the wave and circulation environment during the oil spill. Oil extent at the water surface was derived from satellite imagery and used to determine initial conditions for a Lagrangian particle tracking model to simulate short-term (less than one week) oil movement. The tracking model is highly efficient, with the capability to transport 11 million particles on an unstructured mesh with 10 million elements in about 5.5min per day of simulation on 256 computational cores.

Comparisons to satellite imagery indicate that the system of models realistically advects the oil in the nearshore. Oil was observed to move along the coastline toward Florida, toward the barrier islands that protect the Mississippi and Alabama coastlines, into the marshes of southern Louisiana, and along the continental shelf toward Texas. The system of models reproduces faithfully these observed features, and there is a good match to imagery when available. When the overlap between observations and predictions is computed, the predictions show an overlap of 60 percent or greater, even after a week of simulated transport.

The oil particle tracking responded best when the SWAN+ADCIRC-computed currents were the sole forcing. When the wind velocities were also included as a direct forcing, the predicted oil transport was exaggerated in both deep and shallow water. During the mid-June evaluation period, the winds pushed too much oil toward the south and west in the deeper Gulf. During Alex, the winds pushed too much oil against the coastline and into the marshes of southern Louisiana. Neither of these responses were observed in the satellite imagery. While the relative contributions of currents and wind velocities to oil transport remain under investigation, these results indicate that an accurate representation of the nearshore circulation may be sufficient to transport oil in this region.

Oil would have penetrated much farther inland if a storm like Katrina had tracked through southeastern Louisiana. Oil would have flowed over and around the barrier islands and covered the marshes and bayou in the region. The city of New Orleans would have been threatened by oil in Lake Pontchartrain and in the Caernarvon and Biloxi marshes to the east, and this oil may have remained long after the storm waters had receded. Alternatively, oil would have flowed farther westward if a storm like Ike had tracked through the Gulf. Strong currents around the Mississippi River delta would have moved oil onto the Louisiana-Texas continental shelf, where it would have moved along the coastline toward Texas.

Future work should focus on an improved description of the physical, biological and chemical processes that transport oil in the nearshore. Three-dimensional circulation is essential in deep water, and it would be helpful on the shelf and in shallow water during periods of significant freshwater dis-

charge and low winds. The oil transport should be coupled directly to the hydrodynamics, and it should include the chemical processes of evaporation, decomposition, emulsification, etc., particularly as the lengths of the simulations are increased. These improvements must be conducted in ways that are both accurate and efficient, so that high-fidelity and timely forecasts can continue to be provided to emergency managers.

6. Acknowledgements

Funding for this work was provided by BP and the Gulf of Mexico Research Initiative, the National Science Foundation Office of Cyber Infrastructure award number 1042314 and the U.S. Department of Homeland Security award number 2008-ST-061-ND0001. The views and conclusions contained in this document are those of the authors and should not be interpreted as necessarily representing the official policies, either expressed or implied, of the U.S. Department of Homeland Security.

References

Adamo, M., De Carolis, G., De Pasquale, V., and Pasquariello, G. (2009). Detection and tracking of oil slicks on sun-glittered visible and near infrared satellite imagery. International Journal of Remote Sensing, 30(24), 6403-6427.

Al-Rabeh, A.H. (1994). Estimating surface oil spill transport due to wind in the Arabian Gulf. Ocean Engineering, 21(5), 461-465.

Alpers, W., and Espedal, H.A. (2004). Oils and surfactants. Synthetic Aperture Radar Marine Users Manual, Jackson, C.R., and Apel, J.R.

[eds], NOAA/NESDIS Office of Research and Applications, 263-276, http://www.sarusersmanual.com/ManualPDF/NOAASARManual_CH11_pg263-276.pdf

ASCE (1996). State-of-the-art review of modeling transport and fate of oil spills. Journal of Hydraulic Engineering, November 1996, pp. 594-609.

Atkinson, J.H., Westerink, J.J., and Hervouet, J.M. (2004). Similarities between the wave equation and the quasi-bubble solutions to the shallow water equations. International Journal for Numerical Methods in Fluids, 45, 689-714.

Audunson, T. (1980). The fate and weathering of surface oil from the Bravo blowout. Marine Environmental Research, 3(1), 35-61.

Azevedo, A., Oliveira, A., Fortunato, A.B., and Bertin, X. (2009). Application of an Eulerian-Lagrangian oil spill modeling system to the Prestige accident: trajectory analysis. Journal of Coastal Research, SI 56, 777-781.

Beegle-Krause, C.J. (1999). GNOME: NOAA's Next-Generation Spill Trajectory Model. Oceans '99 MTS/IEEE Proceedings. Escondido, CA: MTS/IEEE Conference Committee. vol. 3: pp. 1262-1266.

Beegle-Krause, C.J. (2001). General NOAA Oil Modeling Environment (GNOME): A New Spill Trajectory Model. IOSC 2001 Proceedings, Tampa, FL, March 26-29, 2001. St. Louis, MO: Mira Digital Publishing, Inc. Vol. 2: pp. 865-871.

Booij, N., Ris, R.C., and Holthuijsen, L.H. (1999). A third-generation wave model for coastal regions, Part I, Model description and validation. Journal of Geophysical Research, 104, 7649-7666.

Bragg, J.R., Prince, R.C., Harner, E.J., and Atlas, R.M. (1994). Effectiveness of bioremediation for the Exxon-Valdez oil-spill. Nature, 368, 413418.

Brekke, C., and Solberg, A.H.S. (2005). Oil spill detection by satellite remote sensing. Remote Sensing of Environment, 95, 1-13.

Brostrom, G., Carrasco, A., Hole, L.R., Dick, S., Janssen, F., Mattsson, J., and Berger, S. (2011). Usefulness of high resolution coastal models for operational oil spill forecast: the 'Full City' accident. Ocean Science, 7, 805-820.

Bunya, S., Dietrich, J.C., Westerink, J.J., Ebersole, B.A., Smith, J.M., Atkinson, J.H., Jensen, R.E., Resio, D.T., Luettich Jr., R.A., Dawson, C.N., Cardone, V.J., Cox, A.T., Powell, M.D., Westerink, H.J., and Roberts, H.J. (2010). A High Resolution Coupled Riverine Flow, Tide, Wind, Wind Wave and Storm Surge Model for Southern Louisiana and Mississippi: Part I - Model Development and Validation. Monthly Weather Review, 138(2), 345-377.

Camilli, R., Reddy, C.M., Yoerger, D.R., Van Mooy, B.A.S., Jakuba, M.V., Kinsey, J.C., McIntyre, C.P., Sylva, S.P., and Maloney, J.V. (2010). Tracking hydrocarbon plume transport and biodegradation at Deepwater Horizon. Science, 330, 201-204.

Castanedo, S., Medina, R., Losada, I.J., Vidal, C., Mendez, F.J., Osorio, A., Juanes, J.A., and Puente, A. (2006). The Prestige oil spill in Cantabria (Bay of Biscay). Part I: Operational forecasting system for quick response, risk assessment, and protection of natural resources. Journal of Coastal Research, 22(6), 1474-1489.

Carr, S.D., Hench, J.L., Luettich Jr., R.A., Forward Jr., R.B., and Tankersley, R.A. (2005). Spatial patterns in the ovigerous blue crab spawning migration: results from a coupled behavioral-physical model. Marine Ecology Progress Series, 294, 213-226.

Chang, Y.-L., Oey, L., Xu, F.-H., Lu, H.-F., and Fujisaki, A. (2011). 2010 oil spill: trajectory projections based on ensemble drifter analyses. Ocean Dynamics, 61, 829-839.

Churchill, J.H., Blanton, B.O., Hench, J.L., Luettich Jr., R.A., and Werner, F.E. (1999). Flood tide circulation near Beaufort Inlet, North Carolina: implications for larval recruitment. Estuaries, 22(4), 1057-1070.

Dawson, C.N., Westerink, J.J., Feyen, J.C., and Pothina, D. (2006). Continuous, Discontinuous and Coupled Discontinuous-Continuous Galerkin Finite Element Methods for the Shallow Water Equations. International Journal for Numerical Methods in Fluids, 52, 63-88.

DeSantis, J. (2010). Half of Terrebonne boom lays idle. The Houma Courier, 22 May 2010.

Diercks, A.-R., Highsmith, R.C., Asper, V.L., Joung, D.J., Zhou, Z., Guo, L., Shiller, A.M., Joye, S.B., Teske, A.P., Guinasso, N., Wade, T.L., and

Lohrenz, S.E. (2011). Characterization of subsurface polycyclic aromatic hydrocarbons at the Deepwater Horizon site. Geophysical Research Letters, 37, L20602.

Dietrich, J.C., Bunya, S., Westerink, J.J., Ebersole, B.A., Smith, J.M., Atkinson, J.H., Jensen, R.E., Resio, D.T., Luettich Jr., R.A., Dawson, C.N., Cardone, V.J., Cox, A.T., Powell, M.D., Westerink, H.J., and Roberts, H.J. (2010). A High Resolution Coupled Riverine Flow, Tide, Wind, Wind Wave and Storm Surge Model for Southern Louisiana and Mississippi: Part II - Synoptic Description and Analyses of Hurricanes Katrina and Rita. Monthly Weather Review, 138, 378-404.

Dietrich, J.C., Zijlema, M., Westerink, J.J., Holthuijsen, L.H., Dawson, C.N., Luettich Jr., R.A., Jensen, R.E., Smith, J.M., Stelling, G.S., and Stone, G.W. (2011a). Modeling Hurricane Waves and Storm Surge using Integrally-Coupled, Scalable Computations. Coastal Engineering, 58, 45-65.

Dietrich, J.C., Westerink, J.J., Kennedy, A.B., Smith, J.M., Jensen, R.E., Zijlema, M., Holthuijsen, L.H., Dawson, C.N., Luettich Jr., R.A., Powell, M.D., Cardone, V.J., Cox, A.T., Stone, G.W., Pourtaheri, H., Hope, M.E., Tanaka, S., Westerink, L.G., Westerink, H.J., and Cobell, Z. (2011b). Hurricane Gustav (2008) Waves, Storm Surge and Currents: Hindcast and Synoptic Analysis in Southern Louisiana. Monthly Weather Review, 139(8), 2488-2522.

Dietrich, J.C., Tanaka, S., Westerink, J.J., Dawson, C.N., Luettich Jr., R.A., Zijlema, M., Holthuijsen, L.H., Smith, J.M., Westerink, L.G.,

and Westerink, H.J. (2011c). Performance of the Unstructured-Mesh, SWAN+ADCIRC Model in Computing Hurricane Waves and Surge. Journal of Scientific Computing, in press.

Ebersole, B.A., Westerink, J.J., Resio, D.T., and Dean, R.G. (2007). Performance Evaluation of the New Orleans and Southeast Louisiana Hurricane Protection System, Volume IV - The Storm. Final Report of the Interagency Performance Evaluation Task Force, U.S. Army Corps of Engineers, Washington, D.C.

Edwards, B.R., Reddy, C.M., Camilli, R., Carmichael, C.A., Longnecker, K., and Van Mooy, B.A.S. (2011). Rapid microbial respiration of oil from the Deepwater Horizon spill in offshore surface waters of the Gulf of Mexico. Environmental Research Letters, 6, 035301.

FEMA (2009). Flood Insurance Study: Southeastern Parishes, Louisiana, Intermediate Submission 2: Offshore Water Levels and Waves, US Army Corps of Engineers, New Orleans District

Fleming, J., Fulcher, C., Luettich Jr., R.A., Estrade, B., Allen, G., and Winer, H. (2008). A Real Time Storm Surge Forecasting System using ADCIRC. Proceedings of Estuarine and Coastal Modeling X, M. L. Spaulding [ed], ASCE, 373-392.

Hanson, J. L., Tracy, B.A., Tolman, H.L., and Scott, R.D. (2009). Pacific hindcast performance of three numerical wave models. Journal of Atmospheric and Oceanic Technology, 26, 16141633.

Hatcher, M. (2010). BP pins its hopes on two-pronged strategy: As it attempts to plug leak, feds OK more aggressive use of dispersants. Houston Chronicle, 15 May 2010.

Hazen, T.C., et al. (2010). Deep-sea oil plume enriches indigenous oil-degrading bacteria. Science, 330, 204-208.

Hope, M.E., Westerink, J.J., Kennedy, A.B., Dietrich, J.C., Dawson, C.N., Bender, C., Smith, J.M., Jensen, R.E., Zijlema, M., Holthuijsen, L.H., Luettich Jr., R.A., Powell, M.D., Cardone, V.J., Cox, A.T., Pourtaheri, H., Roberts, H.J., Atkinson, J.H., Tanaka, S., Westerink, H.J., and Westerink, L.G. (2011). Hindcast and Validation of Hurricane Ike (2008) Waves, Forerunner, and Storm Surge. Monthly Weather Review, in preparation.

Janjic, Z. I., Gerrity Jr., J.P., and Nickovic, S. (2001). An Alternative Approach to Nonhydrostatic Modeling. Monthly Weather Review, 129, 1164-1178.

Janjic, Z. I. (2003). A Nonhydrostatic Model Based on a New Approach. Meteorology and Atmospheric Physics, 82, 271-285.

Kennedy, A.B., Gravois, U., Zachry, B.C., Westerink, J.J., Hope, M.E., Dietrich, J.C., Powell, M.D., Cox, A.T., Luettich Jr., R.A., and Dean, R.G. (2011). Origin of the Hurricane Ike Forerunner Surge. Geophysical Research Letters, 38, L08608, doi:10.1029/2011GL047090.

Kessler, J.D. (2011). A persistent oxygen anomaly reveals the fate of spilled methane in the deep Gulf of Mexico. Science, 331, 212-315.

Kolar, R.L., Westerink, J.J., Cantekin, M.E., and Blain, C.A. (1994a). Aspects of nonlinear simulations using shallow water models based on the wave continuity equations. Computers and Fluids, 23(3), 1-24.

Kolar, R.L., Westerink, J.J., Gray, W.G., and Luettich, R.A. (1994b). Shallow-water modeling in spherical coordinates: Equation formulation, numerical implementation, and application. Journal of Hydraulic Research, 32(1), 3-24.

Kostka, J.E., Prakash, O., Overholt, W.A., Green, S.J., Freyer, G., Canion, A., Delgardio, J., Norton, N., Hazen, T.C., and Huettel, M. (2011). Hydrocarbon-Degrading Bacteria and the Bacterial Community Response in Gulf of Mexico Beach Sands Impacted by the Deepwater Horizon Oil Spill. Appl. Environ. Microbiol., 77(22), 7962-7974.

Kujawinski, E.B., Kido Soule, M.C., Valentine, D.L., Boysen, A.K., Longnecker, K., and Redmond, M.C. (2011). Fate of Dispersants Associated with the Deepwater Horizon Oil Spill. Environmental Science & Technology, 45, 1298-1306.

Lindstrom, J. E., et al. (1991). Microbial-populations and hydrocarbon biodegradation potentials in fertilized shoreline sediments affected by the T/V Exxon-Valdez oil-spill. Appl. Environ. Microbiol., 57, 25142522.

Liu, Y., Weisberg, R.H., Hu, C., and Zheng, L. (2011a), Tracking the Deepwater Horizon oil spill: A modeling perspective. Eos Trans. AGU, 92(6), 4546, doi:10.1029/2011EO060001.

Liu, Y., Weisberg, R.H., Hu, C., and Zheng, L. (2011). Combining numerical ocean circulation models with satellite observations in a trajectory forecast system: a rapid response to the Deepwater Horizon oil spill. Proceedings of SPIE, 8030.

Lubchenco J., McNutt, M., Lehr, B., Sogg, M., Miller, M., Hammond, S., and Conner, W. (2010). Deepwater Horizon/BP Oil Budget: what happened to the oil? National Oceanic and Atmospheric Administration Report. Silver Spring, MD.

Luettich Jr., R.A., Hench, J.L., Williams, C.D., Blanton, B.O., and Werner, F.E. (1998). Tidal circulation and larval transport through a barrier island inlet. Estuarine and Coastal Modeling V, M. Spaulding et al. [eds], ASCE, 849-863

Luettich, R.A., and Westerink, J.J. (2004). Formulation and Numerical Implementation of the 2D/3D ADCIRC Finite Element Model Version 44.XX, `http://adcirc.org/adcirc_theory_2004_12_08.pdf`.

Maltrud, M., Peacock, S., and Visbeck, M. (2010) On the possible long-term fate of oil released in the Deepwater Horizon incident, estimated using ensembles of dye release simulations. Environmental Research Letters, 5(3).

Mariano, A.J., Kourafalou, V.H., Srinivasan, A., Kang, H., Halliwell, G.R., Ryan, E.H., and Roffer, M. (2011). On the modeling of the 2010 Gulf of Mexico Oil Spill. Dynamics of Atmospheres Oceans, 52, 322-340.

Mukai A.Y., Westerink, J.J., Luettich Jr., R.A., and Mark, D. (2002). Eastcoast 2001: a tidal constituent database for the western North Atlantic,

Gulf of Mexico and Caribbean Sea. US Army Engineer Research and Development Center, Coastal and Hydraulics Laboratory, Technical Report, ERDC/CHL TR-02-24, September 2002, 201p.

National Commission on the BP Deepwater Horizon Oil Spill and Offshore Drilling (NCBPDWHOSOD) (2011). Deepwater: The Gulf oil disaster and the future of offshore drilling, Final report. http://www.oilspillcommission.gov/final-report

National Oceanic and Atmospheric Administration (NOAA) (2010). Satellite derived surface oil analysis products - Deepwater Horizon. http://www.ssd.noaa.gov/PS/MPS/deepwater.html.

National Park Service (2010). Response To Oil On Gulf Island Beaches Continues. Press release, 4 June 2010, http://www.nps.gov/applications/digest/headline.cfm?type=Incidents&id=5117.

Oliveira, A., Fortunato, A.B., and Pinto, L. (2006). Modeling the hydrodynamics and the fate of passive and active tracers in the Guadiana estuary. Estuarine, Coastal and Shelf Science, 70, 76-84.

Pasch, R.J. (2010). Tropical Cyclone Report: Hurricane Alex (AL012010). National Hurricane Center, 15 December 2010.

Powell, M., and Houston, S. (1996). Hurricane Andrews landfall in south Florida. Part II: Surface wind fields and potential realtime applications. Weather and Forecasting, 11, 329349.

Proctor, R., Flather, R.A., and Elliott, A.J. (1994). Modelling tides and surface drift in the Arabian Gulf - application to the Gulf oil spill. Continental Shelf Research, 14(5), 531-545.

Reed, M., Turner, A., Odulo, T., Isaji, S., Sortrom, S. and Mathisen, J.O. (1990). Field evaluation of satellite-tracked surface drifting buoys in simulating the movement of spilled oil in the marine environment. U.S. Department of the Interior, Minerals Management Service, MMS 90-0050.

Reed, M., Turner, C., and Odulo, A. (1994). The role of wind and emulsification in modelling oil spill and surface drifter trajectories. Spill Science & Technology Bulletin, 1(2), 143-157.

Reed, M., Johansen, O., Brandvik, P.J., Daling, P., Lewis, A., Fiocco, R., Mackay, D., and Prentki, R. (1999). Oil Spill Modeling towards the Close of the 20th Century: Overview of the State of the Art. Spill Science & Technology Bulletin, 5(1), 3-16.

Resio, D.T., and Westerink, J.J. (2008). Modeling the Physics of Storm Surges. Physics Today, 61, 9, 33-38.

Reyns, N.B., Eggleston, D.B., and Luettich Jr., R.A. (2006). Secondary dispersal of early juvenile blue crabs within a wind-driven estuary. Limnology and Oceanography, 51(5).

Robertson, C., and Krauss, C. (2010). Gulf Spill is the Largest of its Kind, Scientists Say. New York Times, 2 August 2010.

Rosenberg, E., et al. (1996). Oil bioremediation using insoluble nitrogen source. J. Biotechnol., 51, 273278.

Samuels, W.B., Huang, N.E., and Amstutz, D.E. (1982). An oilspill trajectory analysis model with a variable wind deflection angle. Ocean Engineering 9(4), 347-360.

Scholz, D.K., Kucklick, J.H., Pond, R., Walker, A.H., Bostrom, A., and Fischbeck, P. (1999). Fate of Spilled Oil in Marine Waters. American Petroleum Institute Publication, 4691, p. 43.

Spaulding, M., (1988). A state-of-the-art review of oil spill trajectory and fate modeling. Oil and Chemical Pollution, 4, 39-55.

Spaulding, M., Anderson, E., Tatsu, I. and Howlett, E. (1993). Simulation of the oil trajectory and fate in the Arabian Gulf from the Mina AI-Ahmadi Spill. Marine Environmental Research, 36(2), 79-115.

Stolzenbach, K.D., Madsen, E.E., Adams, A., Pollack, A. and Cooper, C. (1977). A review and evaluation of basic technique for predicting the behavior of surface oil slicks. Report No. 22, Department of Civil Engineering, Massachusetts Institute of Technology, Cambridge, Massachusetts.

USACE (2009). Hydraulics and Hydrology Appendix, Louisiana Coastal Protection and Restoration: Final Technical Report, US Army Engineer District, New Orleans, LA, 389 pp.

Valentine, D.L., et al. (2010). Propane respiration jump-starts microbial response to a deep oil spill. Science, 330, 208-211.

Van Cooten, S., and 41 co-authors (2011). The CI-FLOW Project: A System for Total Water Level Prediction From the Summit to the

Sea. Bulletin of the American Meteorological Society, in press, doi: 10.1175/2011BAMS3150.1.

Westerink, J.J., Luettich Jr., R.A., Feyen, J.C., Atkinson, J.H., Dawson, C.N., Roberts, H.J., Powell, M.D., Dunion, J.P., Kubatko, E.J., Pourtaheri, H. (2008). A Basin to Channel Scale Unstructured Grid Hurricane Storm Surge Model Applied to Southern Louisiana. Monthly Weather Review, 136, 3, 833-864.

Youssef, M.M. (1993). The Behavior of the Near Ocean Surface under the Combined Action of Waves and Currents in Shallow Water. PhD Dissertation, University of Rhode Island.

Zijlema, M. (2010). Computation of wind-wave spectra in coastal waters with SWAN on unstructured grids. Coastal Engineering, 57, 267-277.

Table 1: Geographic location by type and number shown in Figure 3a.

Cities	1	New Orleans, LA
	2	Pascagoula, MS
	3	Pensacola, FL
Bays, lakes and sounds	4	Terrebonne Bay
	5	Timbalier Bay
	6	Barataria Bay
	7	Lake Pontchartrain
	8	Lake Borgne
	9	Chandeleur Sound
	10	Bay St. Louis
	11	Mississippi Sound
	12	Mobile Bay
	13	Pensacola Bay
Islands and marshes	14	Grand Isle
	15	Caernarvon Marsh
	16	Biloxi Marsh
	17	Chandeleur Islands
	18	Mississippi Sound Islands

Table 2: Summary of satellite sensors that SAB analysts used to generate NOAA's surface oil product.

Satellite(s)	Sensor(s)	Type	Resolution	Number of images used		Owner/operator
				13-23 June	29 July to 5 August	
RADARSAT-1	SAR	C-band SAR	50m	5	3	CSA
RADARSAT-2	SAR	C-band SAR	8m	1	-	CSA, and MacDonald Dettwiler and Associates Ltd
RADARSAT-2	SAR	C-band SAR	50m	1	2	”
Cosmo-SkyMed 1,2,3	SAR	X-band SAR	30m	6	6	ISA
Cosmo-SkyMed 1,2,3	SAR	X-band SAR	100m	1	2	”
TerraSAR-X	SAR	X-band SAR	1m	1	-	DLR, and Astrium
TerraSAR-X	SAR	X-band SAR	3m	-	2	DLR, and Astrium
ALOS	PALSAR	L-band SAR	100m	1	2	JAXA, and Japan Resources Observation System Organization
ALOS	AVNIR-2	Multispectral	10m	-	-	”
ENVISAT	ASAR	C-band SAR	50m	7	4	ESA
ENVISAT	MERIS	Multispectral	260-1200m	-	1	”
Terra and Aqua	MODIS	Multispectral	250m	3	1	NASA
NOAA 15,17,19	AVHRR	Multispectral	1090m	-	-	”
Disaster Monitoring Constellation	UK-DMC, AISAT-1, NigeriaSat-1, Beijing-1	Multispectral	32m	-	-	DMC International Imaging Ltd with UK, Algeria, Turkey and China
SPOT	SPOT 4,5	Multispectral	10-20m	-	-	SPOT Image, and CNES

Table 3: Summary of available satellite imagery during the mid-June analysis period.

Date/Time (UTC)	Satellite/Sensor	Mode (SAR)	Size (m)	Comments
2010/06/13/1548	Envisat ASAR	Wide swath, VV	50	Slick cut off at 28°N.
2010/06/14/1151	Cosmo SkyMed	ScanSAR, VV	30	Low winds create uncertainty on perimeter.
2010/06/15/1151	Radarsat 1	Narrow beam, VV	50	Low winds southwest of Mobile Bay.
2010/06/15/2341	Radarsat 1	Narrow beam, HH	50	
2010/06/16/0336	Envisat ASAR	ScanSAR, VV	50	Missing offshore of AL.
2010/06/16/1555	Envisat ASAR	Wide swath, VV	50	Many areas of low wind.
2010/06/17/1140	Radarsat 1	ScanSAR, HH	50	Florida coast only; low winds near coast.
2010/06/17/1157	Cosmo SkyMed	ScanSAR, VV	30	Low winds, noise give lower confidence.
2010/06/18/0038	Cosmo SkyMed	ScanSAR, VV	30	Crisp delineation along Florida coast only.
2010/06/18/1109	Cosmo SkyMed	ScanSAR, VV	30	Low winds obscure detection; coverage gaps.
2010/06/18/1637	MODIS		250	Clouds near well site.
2010/06/19/0341	Envisat ASAR	Wide swath, VV	50	Low winds in south and far east.
2010/06/19/1601	Envisat ASAR	Wide swath, VV	50	Low winds and scattered convection.
2010/06/19/1856	MODIS		250	Good sun glint, but cloudy near Mobile Bay.
2010/06/19/2324	Radarsat 1	ScanSAR, HH	50	Very clear, but straight edges indicate cut-off.
2010/06/19/2338	Cosmo SkyMed	ScanSAR, VV	30	Calm winds obscured spill edge in deep water.
2010/06/20/1144	Cosmo SkyMed	Huge region, VV	100	Good near Florida coast; convection at 29°N.
2010/06/20/1152	Radarsat 1	ScanSAR, HH	50	Good coverage; clouds hinder delineation.
2010/06/20/2340	TerraSAR-X	Spotlight, VV	1	Coverage of only 100mi^2.
2010/06/20/2357	Radarsat 2	Fine beam, VV	8	Small size; coverage centered on delta.
2010/06/21/1613	ALOS PALSAR	ScanSAR, VV	100	Shows most of slick from LA to FL.
2010/06/21/2326	Cosmo SkyMed	ScanSAR, VV	30	Convection interference obscures shoreline.
2010/06/22/0348	Envisat ASAR	ScanSAR, VV	50	Good coverage; low winds obscure west.
2010/06/22/1147	Radarsat 2	Narrow beam, VV	50	Convection hindered slick delineation.
2010/06/22/1606	Envisat ASAR	Wide swath, VV	50	Slicks in Barataria Bay, primarily.
2010/06/23/1654	MODIS		250	Good coverage near AL and FL coasts.

Table 4: Summary of available satellite imagery during the Hurricane Alex analysis period.

Date/Time (UTC)	Satellite/Sensor	Mode (SAR)	Size (m)	Comments
2010/06/29/0044	Cosmo SkyMed	ScanSAR, VV	30	Slick cut off along eastern edge.
2010/06/29/1546	Envisat ASAR	ScanSAR, VV	50	Good eastern extent; high winds.
2010/06/29/2332	Radarsat 1	ScanSAR, HH	50	Some uncertainty in far west.
2010/06/30/1150	Cosmo SkyMed	Huge region, VV	100	Stringy slicks south of Pensacola Bay.
2010/06/30/1200	Radarsat 1	ScanSAR, HH	50	Western oil extent; convection south of delta.
2010/06/30/2344	Cosmo SkyMed	ScanSAR, VV	30	Good delineation along western edge.
2010/07/01/0005	Radarsat 2	ScanSAR, VV	50	Storms reduce confidence south of delta.
2010/07/01/1209	Cosmo SkyMed	ScanSAR, VV	30	Slicks delineated near MS and AL, delta.
2010/07/01/1626	ALOS PALSAR	ScanSAR, VV	100	Low winds obscure oil along MS coast.
2010/07/01/2340	TerraSAR-X	Stripmap, VV	3	Coastal oil along AL and FL coasts.
2010/07/02/0332	Envisat ASAR	Wide swath, VV	50	Eastern edge of oil near Panama City, FL.
2010/07/02/1156	Radarsat 2	Narrow beam, VV	50	Low confidence southwest of delta.
2010/07/02/1552	Envisat ASAR	Wide swath, VV	50	Good delineation near shore.
2010/07/02/2332	Cosmo SkyMed	Huge region, VV	100	Easternmost oil south of Pensacola, FL.
2010/07/03/0002	Cosmo SkyMed	ScanSAR, VV	30	Low winds obscure bays along LA coast.
2010/07/03/1156	Cosmo SkyMed	ScanSAR, VV	30	Good delineation near shore.
2010/07/03/1612	ALOS PALSAR	ScanSAR, VV	100	East of Mobile Bay, few slicks offshore.
2010/07/04/1144	Radarsat 1	ScanSAR, HH	50	Few slicks south of Pensacola, FL.
2010/07/04/1216	TerraSAR-X	Stripmap, VV	3	Low confidence; few slicks; tiny area.
2010/07/04/1628	MERIS		300	Extensive cloud cover near north shoreline.
2010/07/04/1637	MODIS		250	Extensive cloud cover near north shoreline.
2010/07/05/0008	Cosmo SkyMed	ScanSAR, VV	30	Westernmost oil slick extent.
2010/07/05/1558	Envisat ASAR	ScanSAR, VV	50	Convection, but good view of small slicks.

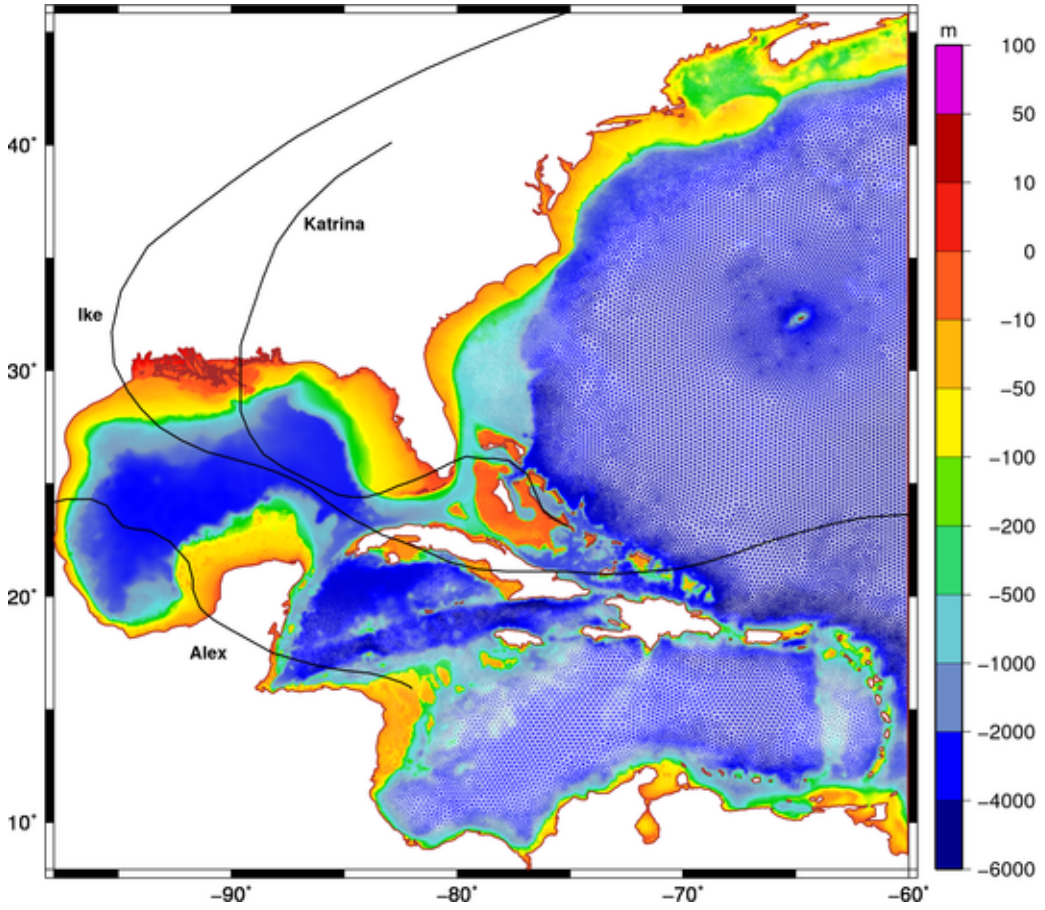

Figure 1: Bathymetry/topography (m) of the SL16 mesh. Hurricane tracks are shown in black lines.

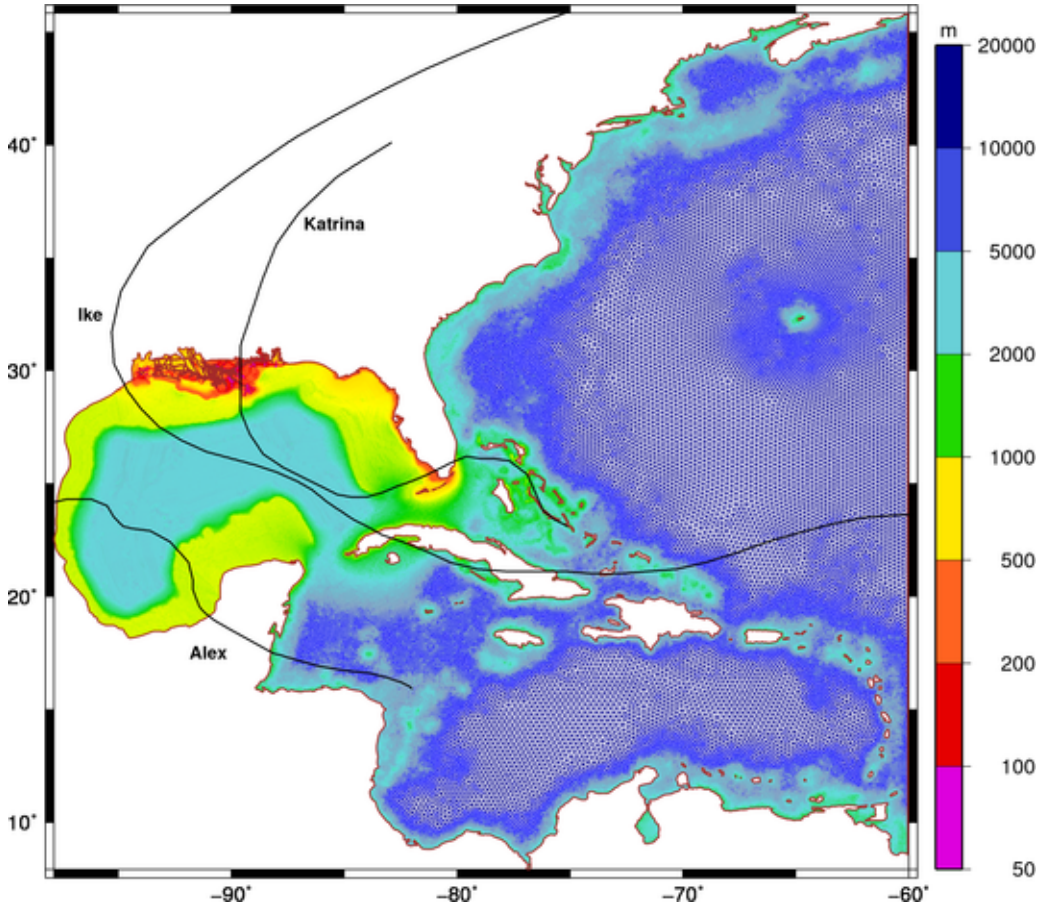

Figure 2: Mesh resolution (m) of the SL16 mesh. Hurricane tracks are shown in black lines.

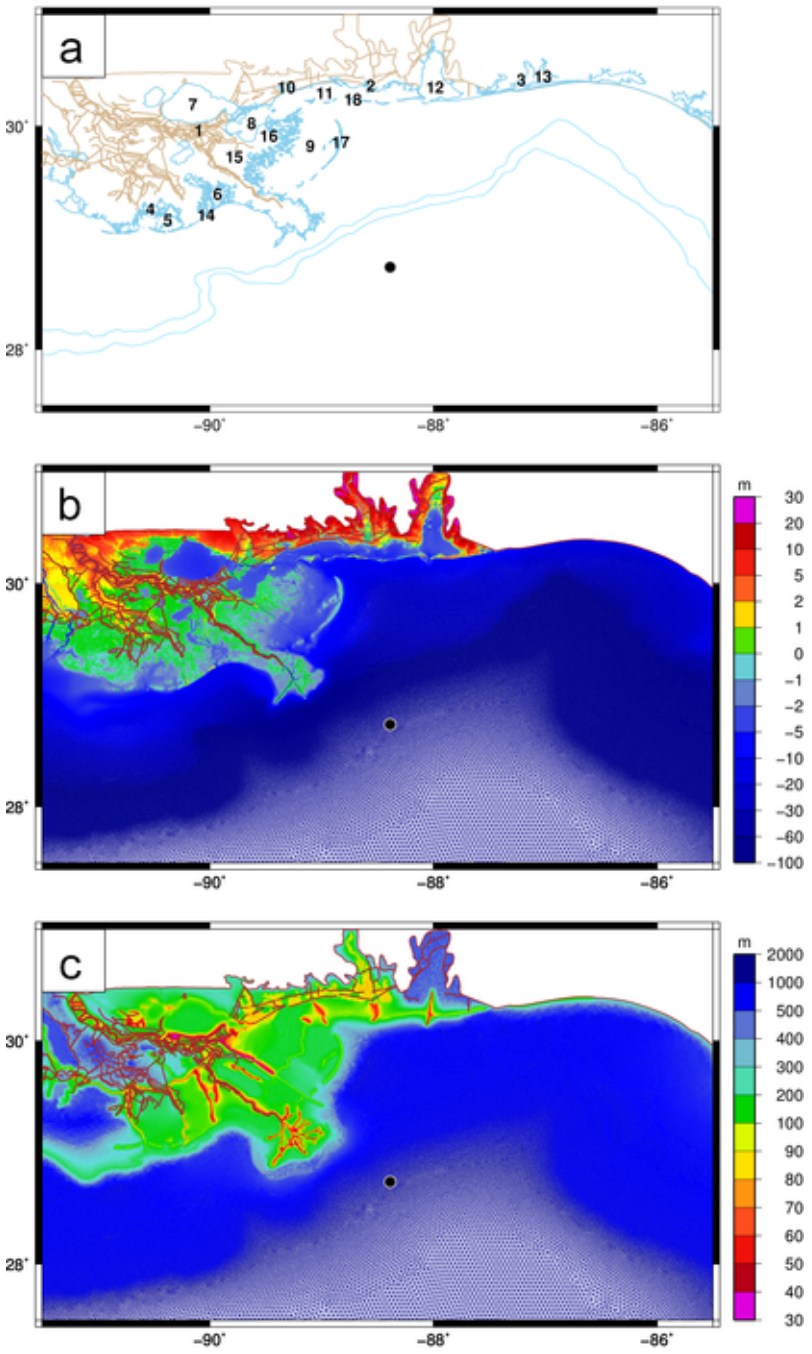

Figure 3: SL16 mesh in the northern Gulf of Mexico, with panels of (a) geographic locations indicated by numbers identified in Table 1, (b) bathymetry/topography (m, relative to NAVD88 2004.65), and (c) mesh resolution (m). The platform location is also indicated.

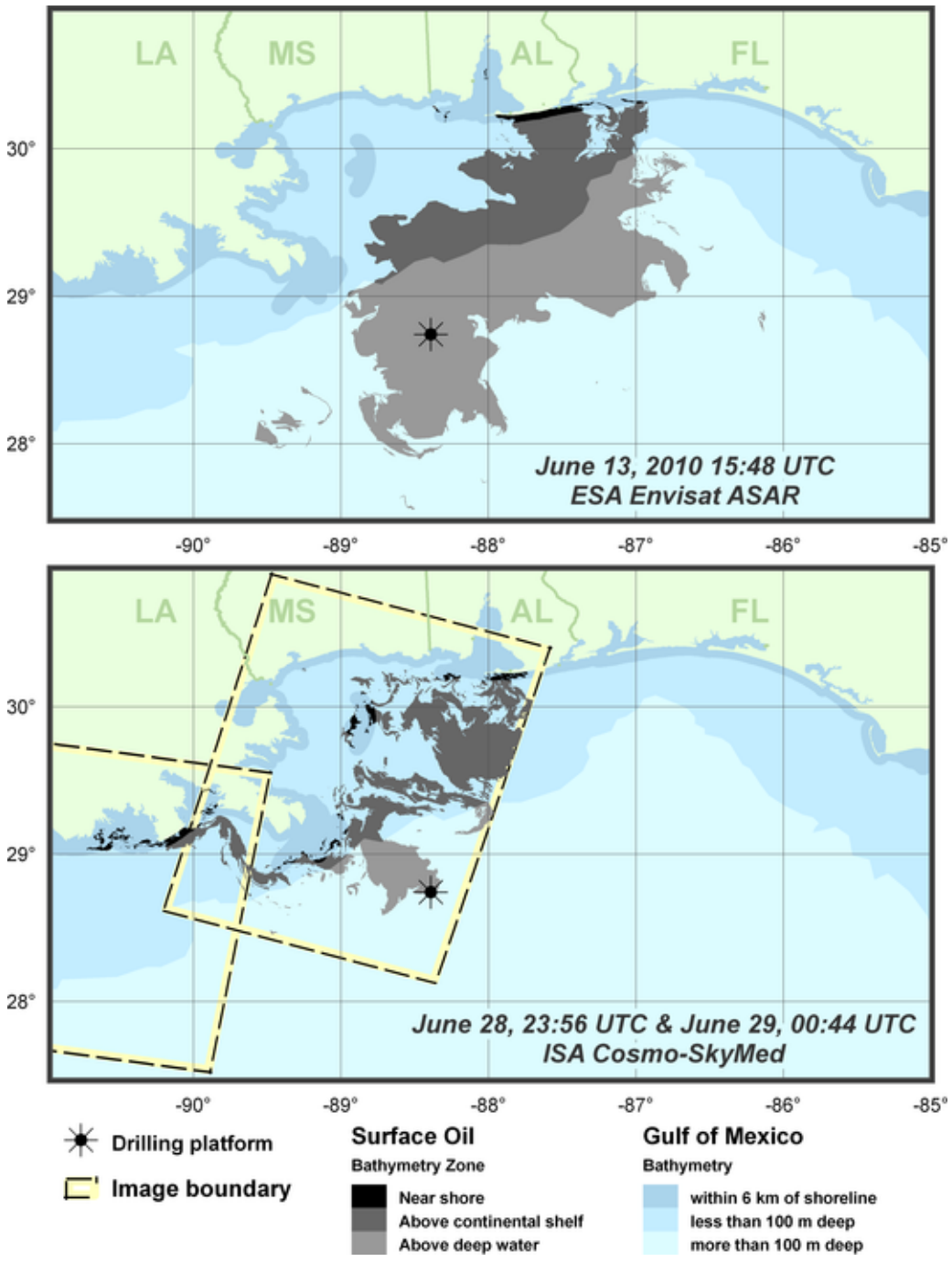

Figure 4: Examples of surface oil delineated by NOAA NESDIS SAB analysts and satellite image coverage for the two sensors used most frequently during the periods of interest.

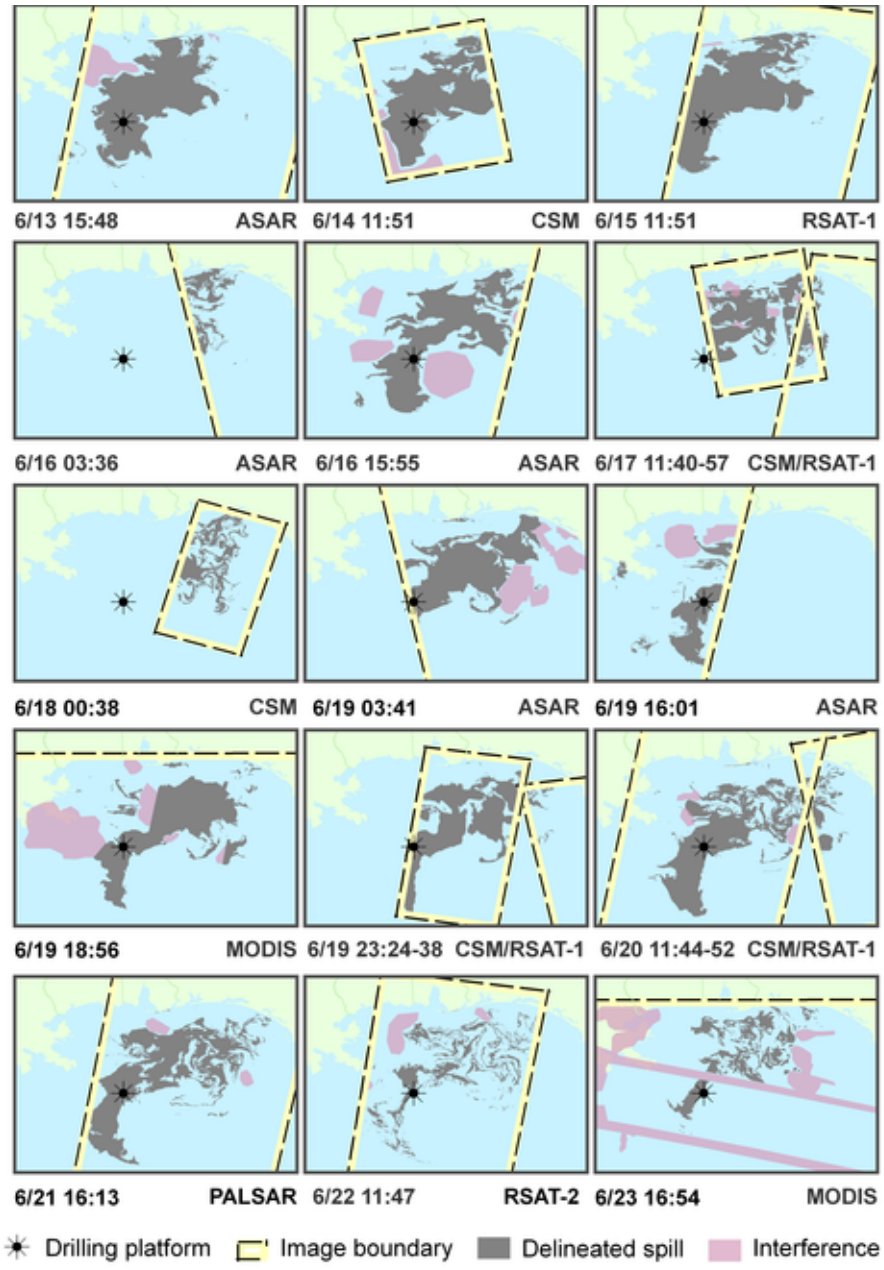

Figure 5: Summary of available satellite imagery during the mid-June time period. The observed spill extents are shown in dark gray, while areas of uncertainty are shown in pink. The platform location and the extents of the satellite imagery are also indicated.

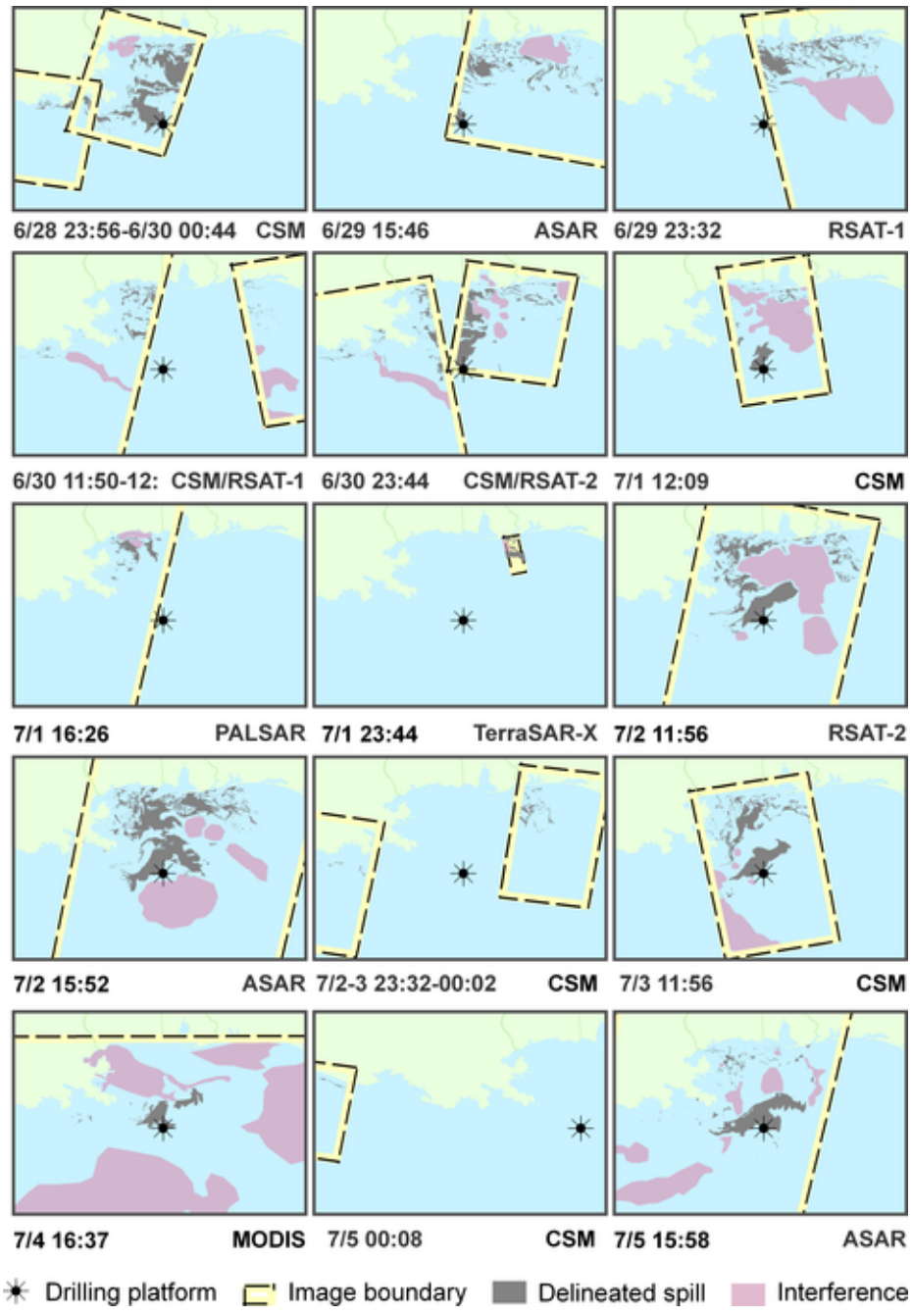

Figure 6: Summary of available satellite imagery during the Alex time period. The observed spill extents are shown in dark gray, while areas of uncertainty are shown in pink. The platform location and the extents of the satellite imagery are also indicated.

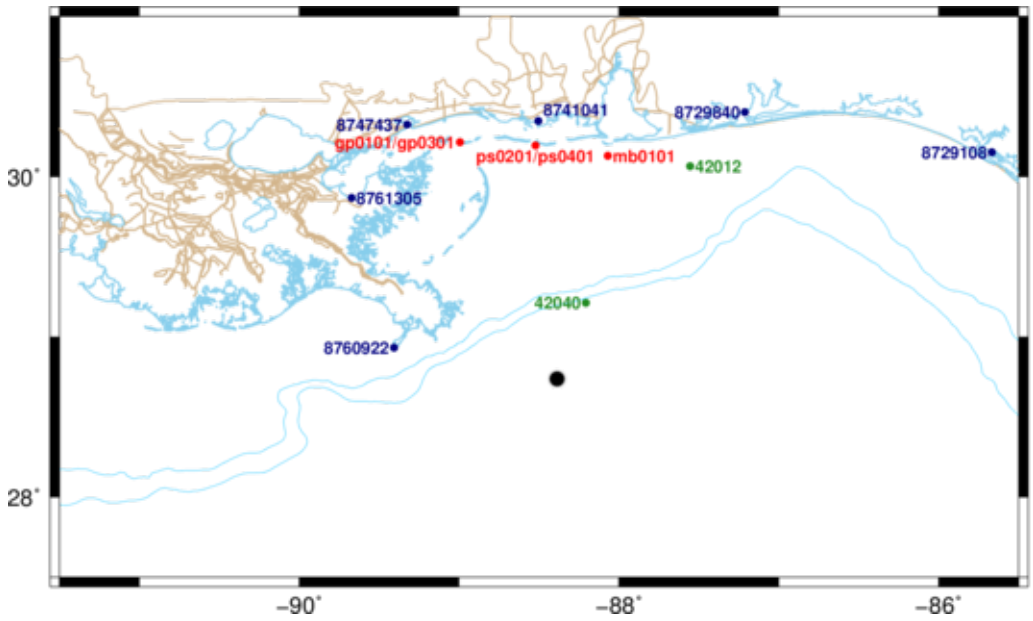

Figure 7: Locations of the NOAA stations that measured winds and water levels (blue) and currents (red), and the NDBC platforms (green) used in the validation of winds and circulation. Blue lines indicate the 0m, 100m and 200m bathymetric contours, while brown lines indicate the SL16 internal road/levee boundaries. The platform location is also indicated.

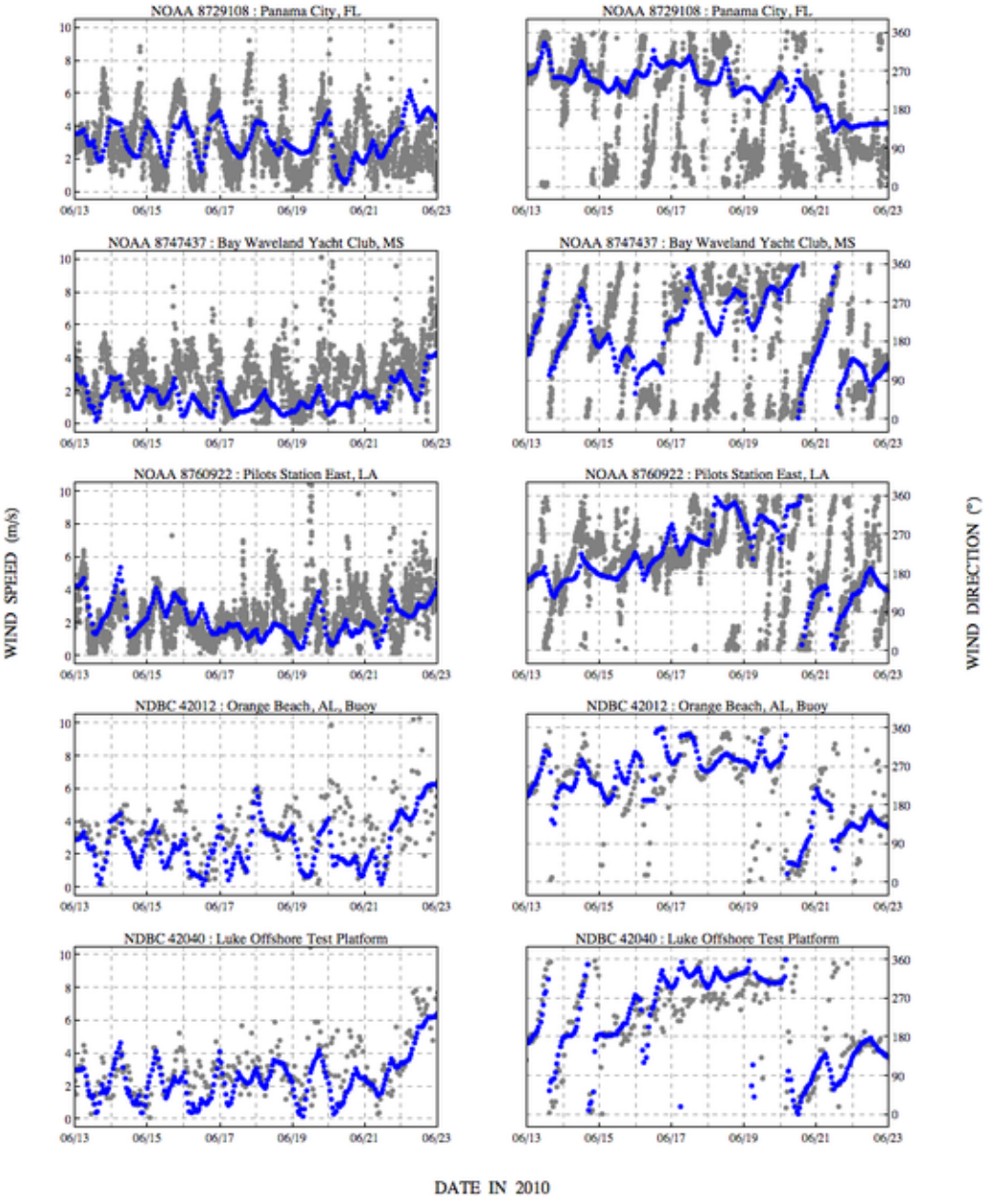

Figure 8: Wind speeds (m s^{-1}) and directions (°, measured clockwise from true north) at selected NOAA stations and NDBC platforms during the mid-June time period. Gray circles are measured data from NOAA and NDBC, while blue circles are wind input to SWAN+ADCIRC. Station locations are shown spatially in Figure 7.

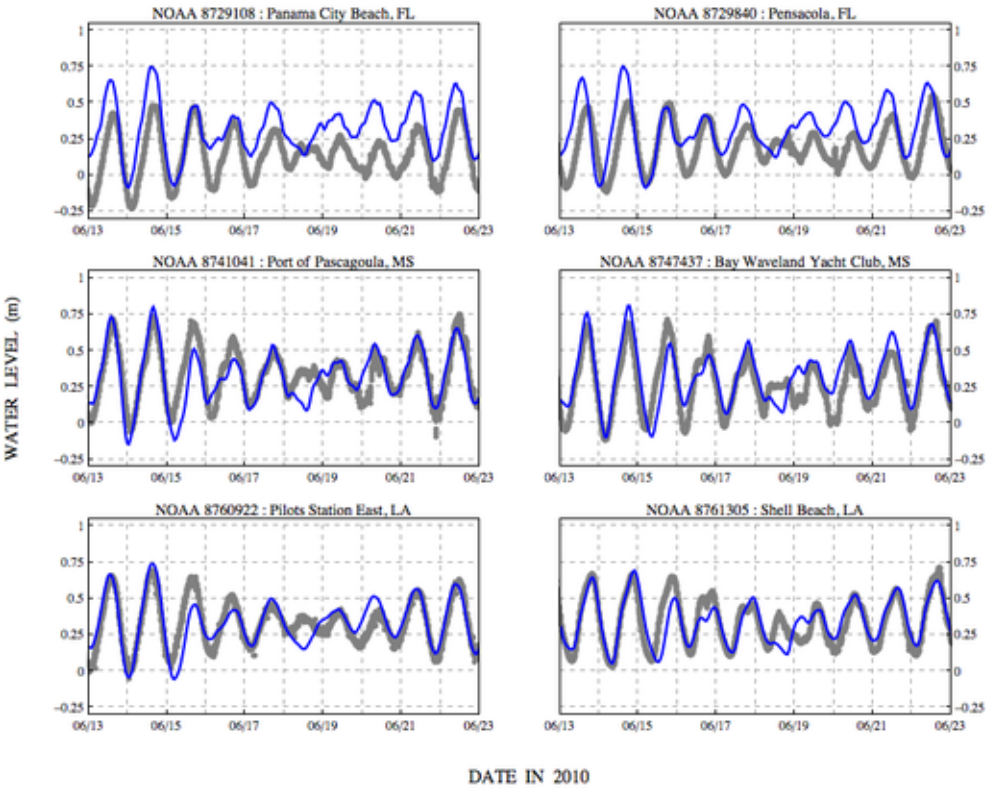

Figure 9: Water levels (m, relative to NAVD88 (2004.65)), at selected NOAA stations during the mid-June time period. Gray circles are measured data from NOAA, while solid blue lines are predicted ADCIRC water levels. Station locations are shown spatially in Figure 7.

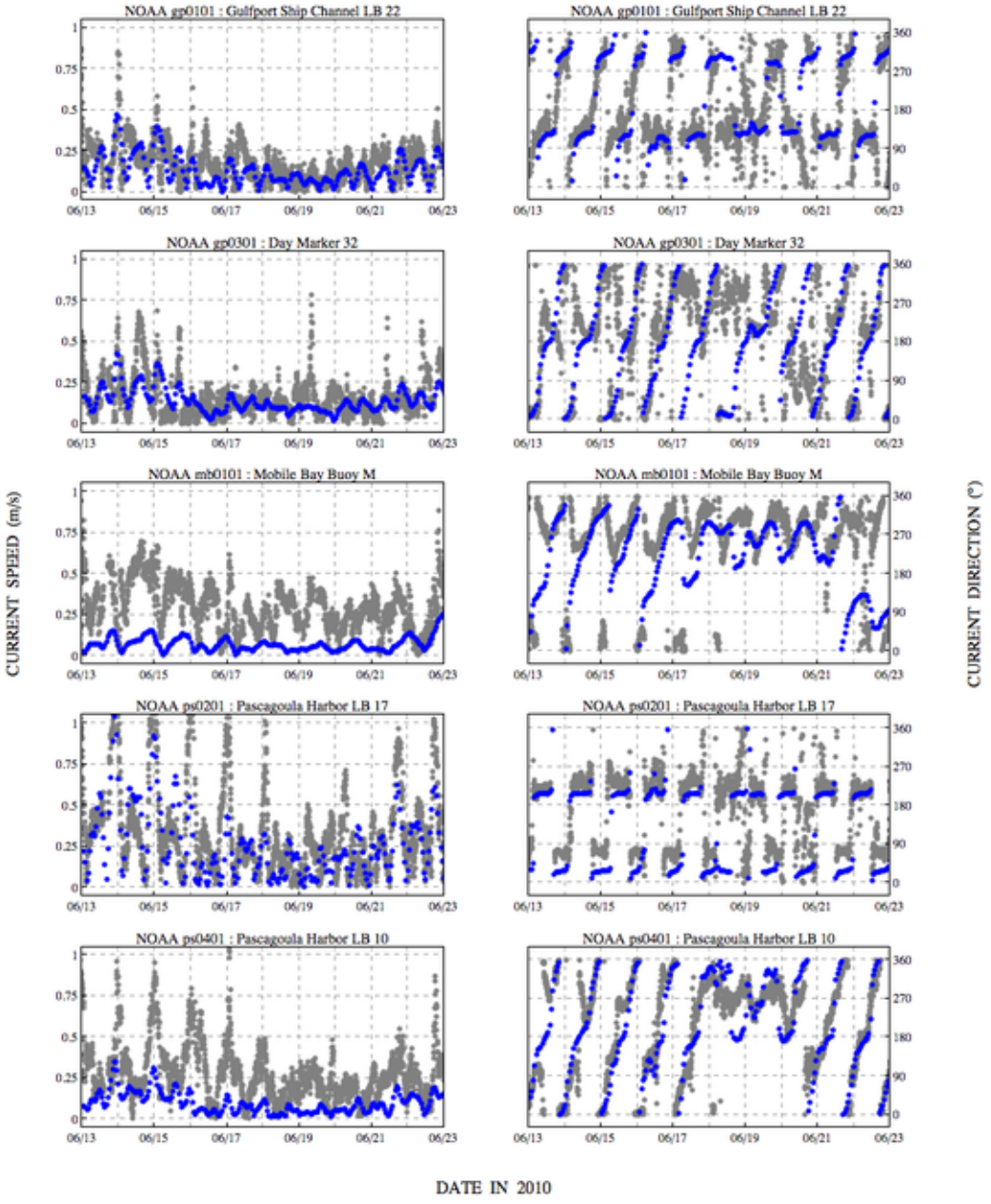

Figure 10: Current speeds (m s^{-1}) and directions (°, measured clockwise from true north) at selected NOAA stations during the mid-June time period. Gray circles are measured data from NOAA, while blue circles are predicted ADCIRC currents. Station locations are shown spatially in Figure 7.

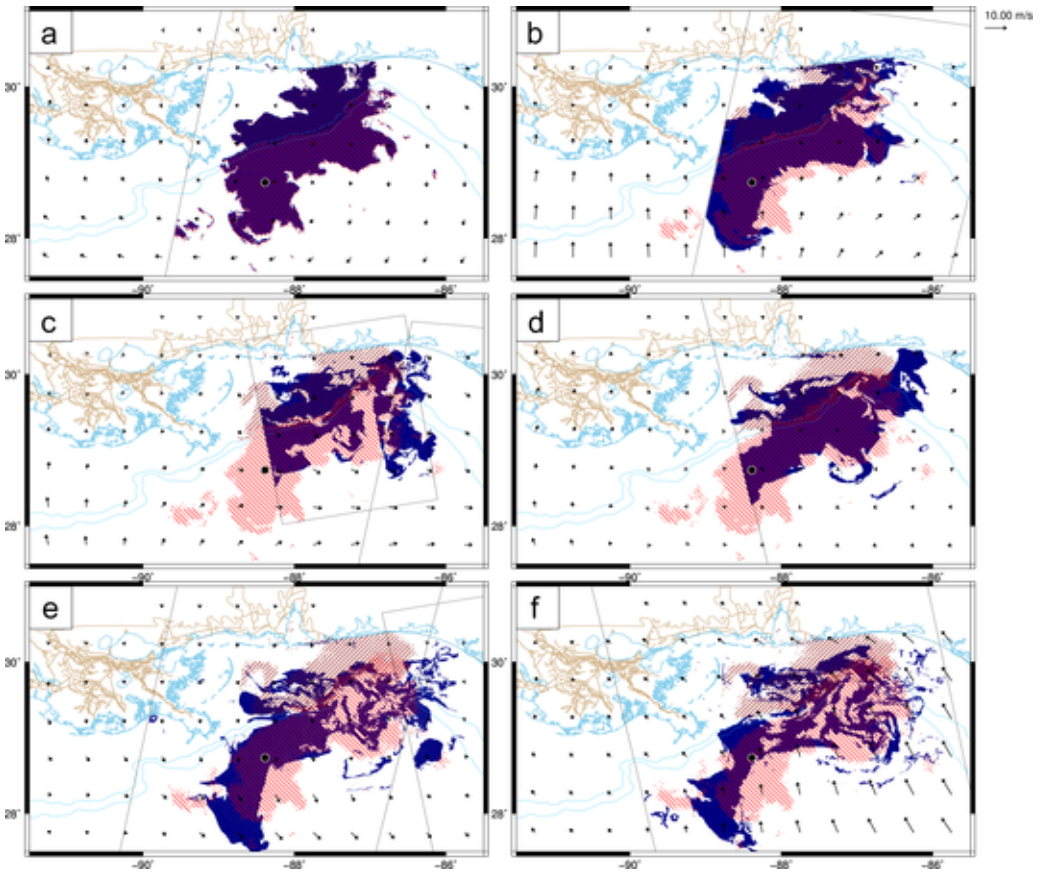

Figure 11: Comparison of observed (solid blue) and predicted (red hatched) oil extents during the mid-June time period, with forcing with currents only ($F_c = 1$ and $F_w = 0$ in Equation 1). A distinction is made between oil that started initially in deep water (light red hatching from northwest to southeast), and oil that started initially on the shelf (dark red hatching from northeast to southwest). The panels are: (a) the initial conditions on 2010/06/13/1548UTC, (b) conditions after 44hr at 2010/06/15/1151UTC, (c) conditions after 92hr at 2010/06/17/1150UTC, (d) conditions after 132hr at 2010/06/19/0341UTC, (e) conditions after 164hr at 2010/06/20/1152UTC, and (f) conditions after 204hr at 2010/06/22/0348UTC. Vectors are wind velocities (m s^{-1}), and the platform location and the extents of the satellite imagery are also indicated.

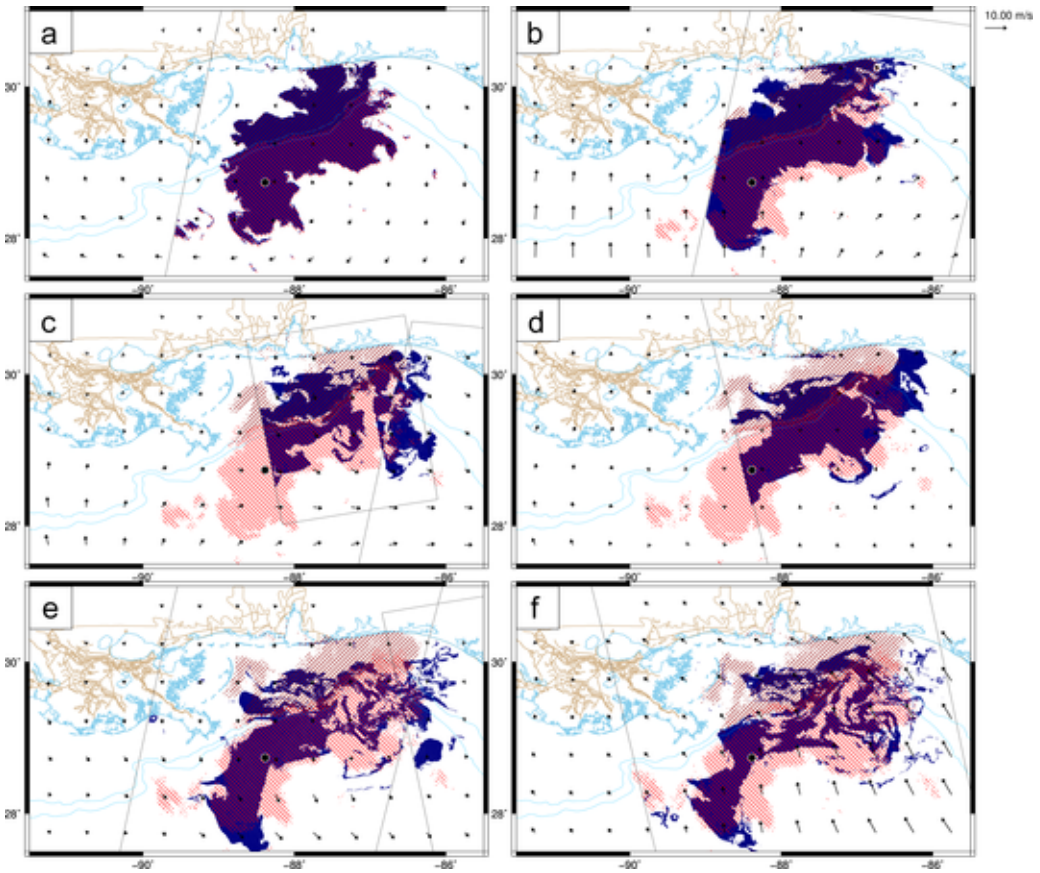

Figure 12: Comparison of observed (solid blue) and predicted (red hatched) oil extents during the mid-June time period, with forcing with currents and winds ($F_c = 1$ and $F_w = 0.01$ in Equation 1). A distinction is made between oil that started initially in deep water (light red hatching from northwest to southeast), and oil that started initially on the shelf (dark red hatching from northeast to southwest). The panels are: (a) the initial conditions on 2010/06/13/1548UTC, (b) conditions after 44hr at 2010/06/15/1151UTC, (c) conditions after 92hr at 2010/06/17/1150UTC, (d) conditions after 132hr at 2010/06/19/0341UTC, (e) conditions after 164hr at 2010/06/20/1152UTC, and (f) conditions after 204hr at 2010/06/22/0348UTC. Vectors are wind velocities (m s^{-1}), and the platform location and the extents of the satellite imagery are also indicated.

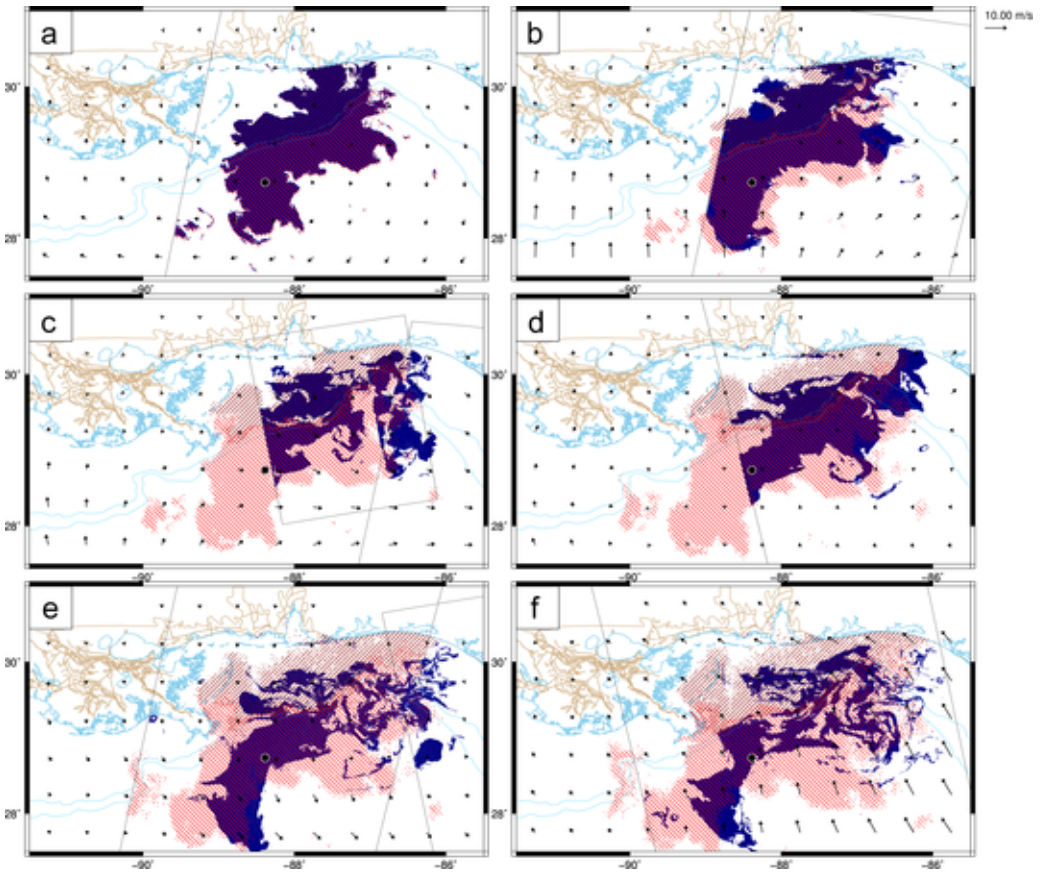

Figure 13: Comparison of observed (solid blue) and predicted (red hatched) oil extents during the mid-June time period, with forcing with currents and winds ($F_c = 1$ and $F_w = 0.03$ in Equation 1). A distinction is made between oil that started initially in deep water (light red hatching from northwest to southeast), and oil that started initially on the shelf (dark red hatching from northeast to southwest). The panels are: (a) the initial conditions on 2010/06/13/1548UTC, (b) conditions after 44hr at 2010/06/15/1151UTC, (c) conditions after 92hr at 2010/06/17/1150UTC, (d) conditions after 132hr at 2010/06/19/0341UTC, (e) conditions after 164hr at 2010/06/20/1152UTC, and (f) conditions after 204hr at 2010/06/22/0348UTC. Vectors are wind velocities (m s^{-1}), and the platform location and the extents of the satellite imagery are also indicated.

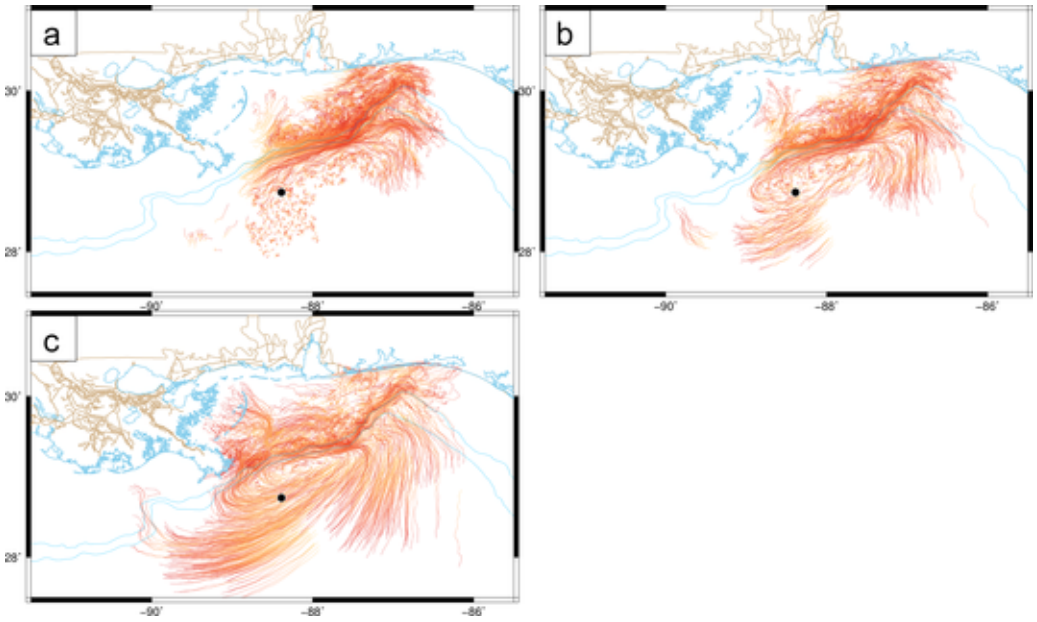

Figure 14: Sampled predicted particle locations in time during the mid-June period, with forcings from: (a) currents only, (b) currents and 1-percent winds, and (c) currents and 3-percent winds. Particle movement is shown with the trajectories moving from orange to red. Blue lines indicate the 0m, 100m and 200m bathymetric contours, while brown lines indicate the SL16 internal boundaries. The platform location is also indicated.

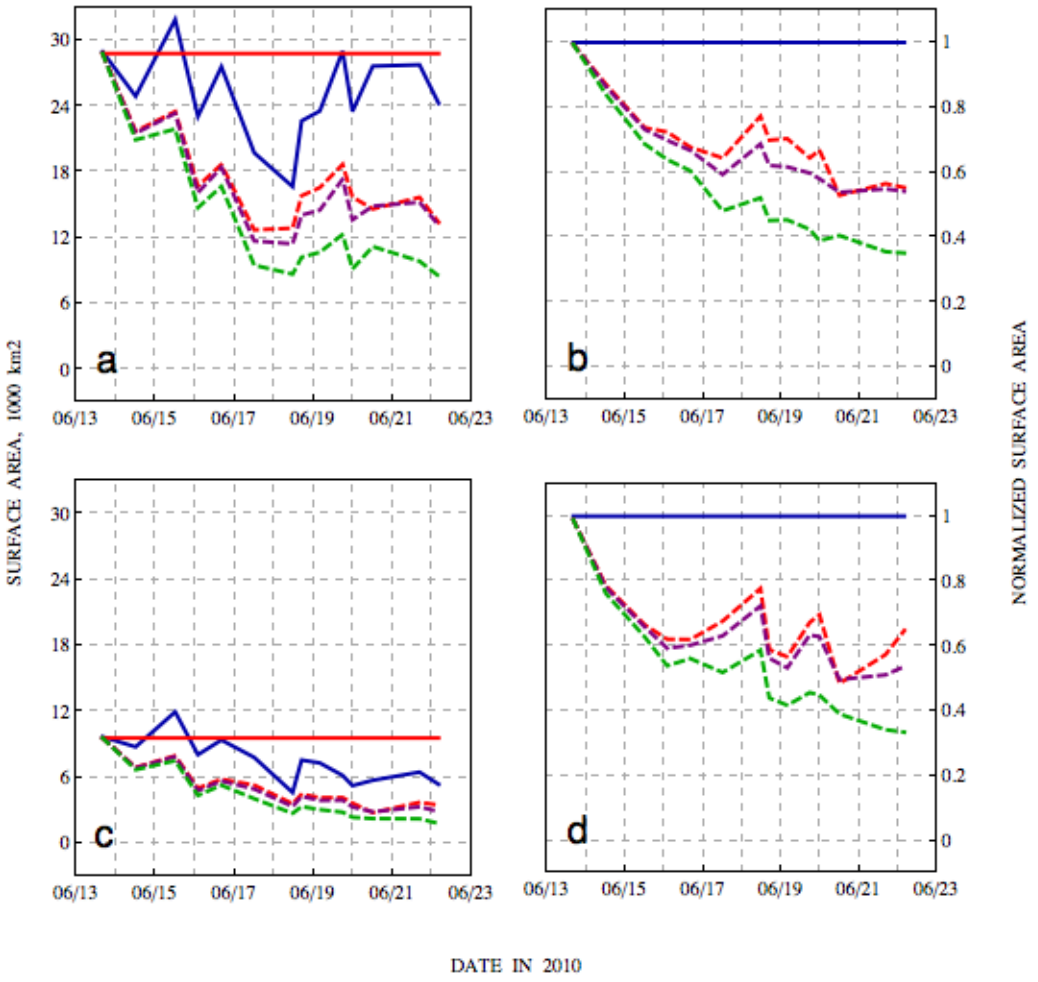

Figure 15: Total surface areas of the observed oil spill (solid blue) and particle tracers (solid red) during the mid-June time period, as well as the overlapping areas from the currents/winds scenarios: currents only (dashed red), currents and 1-percent winds (dashed purple), and currents and 3-percent winds (dashed green). The panels are: (a) areas in 1000km^2 and (b) normalized areas for oil everywhere, as well as (c) areas in 1000km^2 and (d) normalized areas for oil only on the continental shelf. In panels (b) and (d), areas are normalized with respect to the observations.

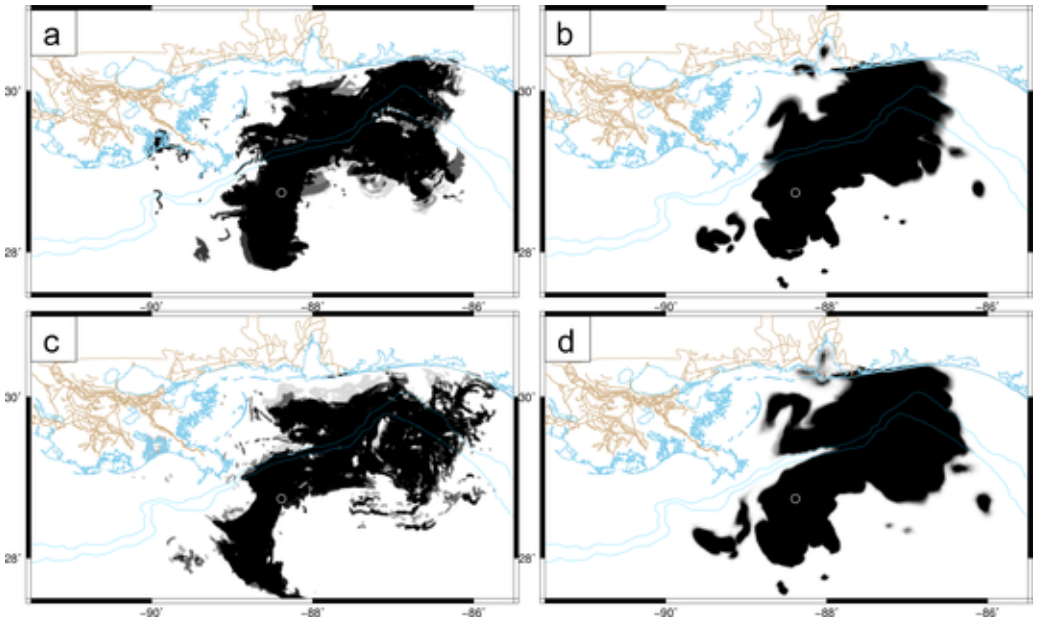

Figure 16: Samples of aggregation of satellite imagery and predicted particle locations (with currents only) during the mid-June time period. Regions without oil are shown in white, while regions with oil are shown in shades of gray and black. The panels are: (a) observations and (b) predictions aggregated over a 24hr window around 2010/06/17/1140 UTC, as well as (c) observations and (d) predictions aggregated over a 24hr window around 2010/06/22/1117 UTC. Blue lines indicate the 0m, 100m and 200m bathymetric contours, while brown lines indicate the SL16 internal road/levee boundaries. The platform location is also indicated.

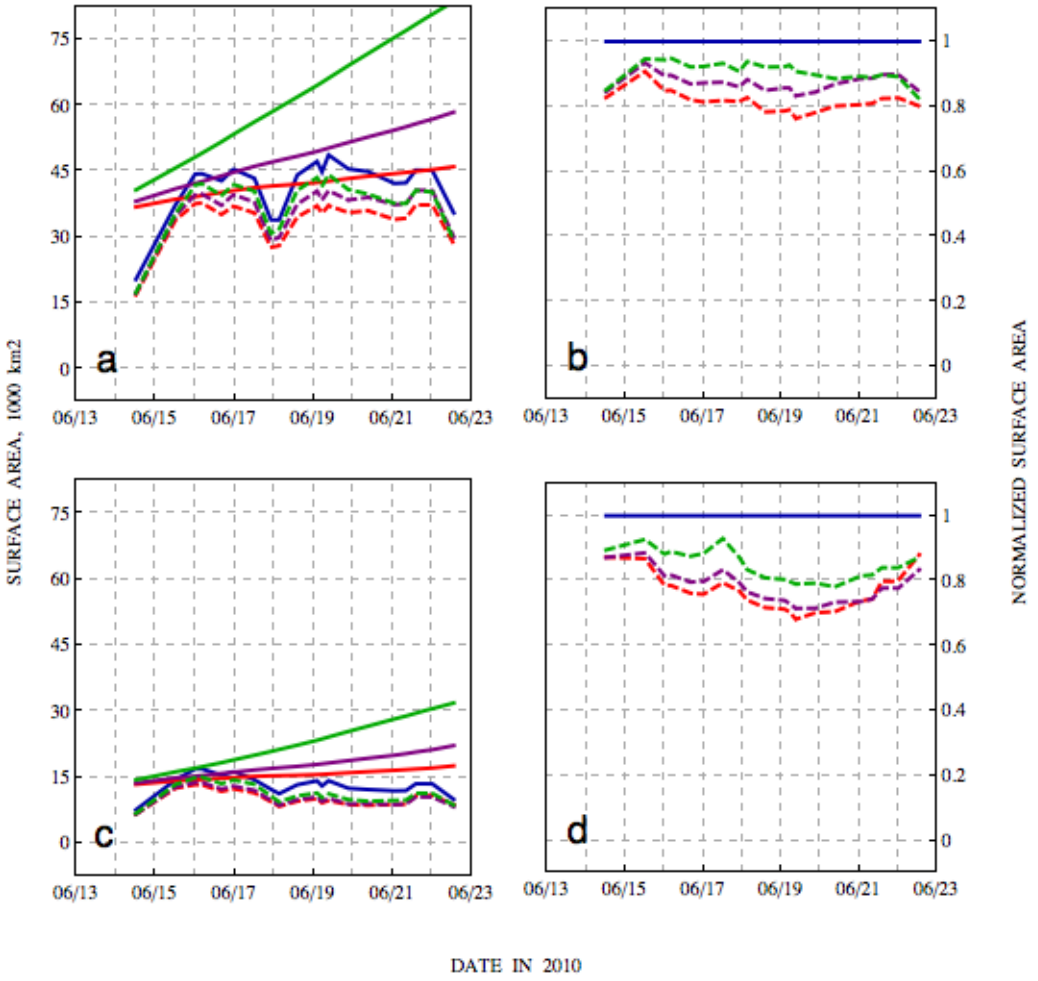

Figure 17: Total surface areas, using the larger aggregation window, of the observed oil spill (solid blue) and particle tracers (solid red, purple and green) during the mid-June time period, as well as the overlapping areas from the currents/winds scenarios: currents only (dashed red), currents and 1-percent winds (dashed purple), and currents and 3-percent winds (dashed green). The panels are: (a) areas in 1000km^2 and (b) normalized areas for oil everywhere, as well as (c) areas in 1000km^2 and (d) normalized areas for oil only on the continental shelf. In panels (b) and (d), areas are normalized with respect to the observations.

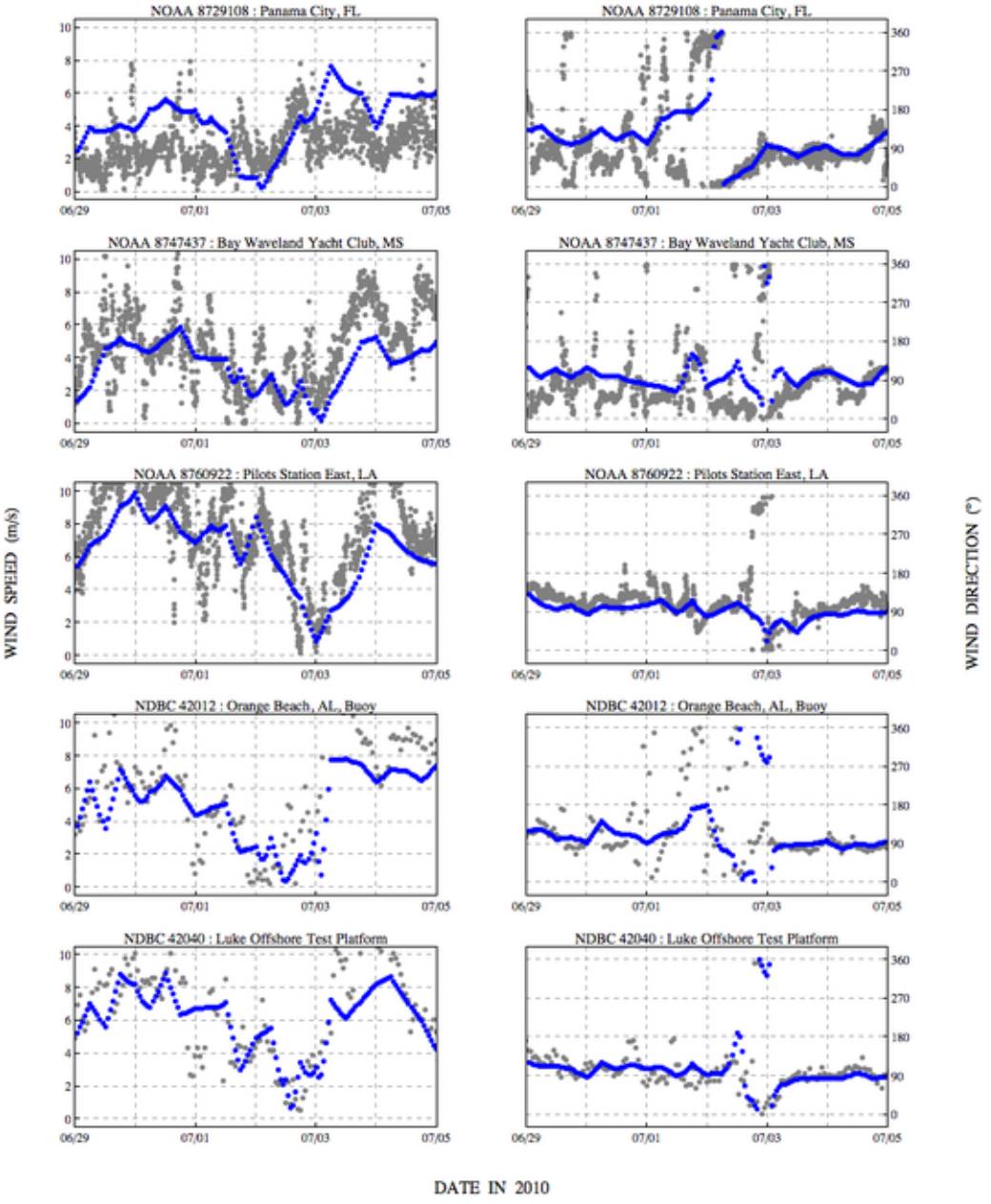

Figure 18: Wind speeds (m s^{-1}) and directions (°, measured clockwise from true north) at selected NOAA stations and NDBC platforms during the Alex time period. Gray circles are measured data from NOAA and NDBC, while blue circles are wind input to SWAN+ADCIRC. Station locations are shown spatially in Figure 7.

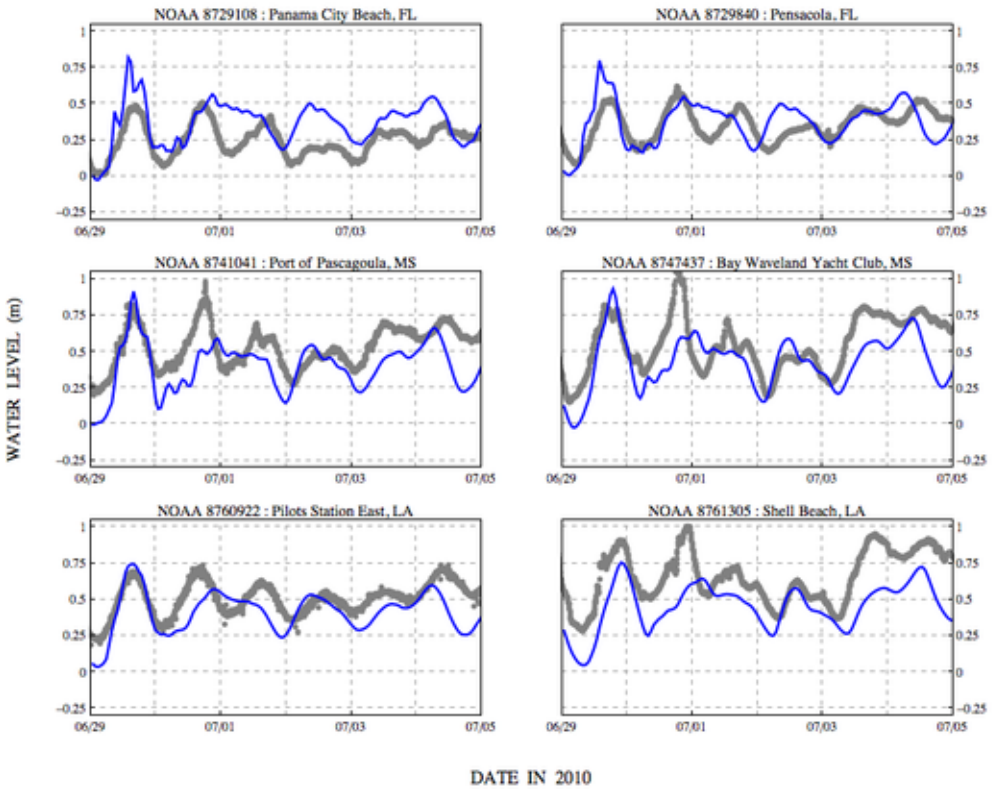

Figure 19: Water levels (m, relative to NAVD88 (2004.65)), at selected NOAA stations during the Alex time period. Gray circles are measured data from NOAA, while solid blue lines are predicted ADCIRC water levels. Station locations are shown spatially in Figure 7.

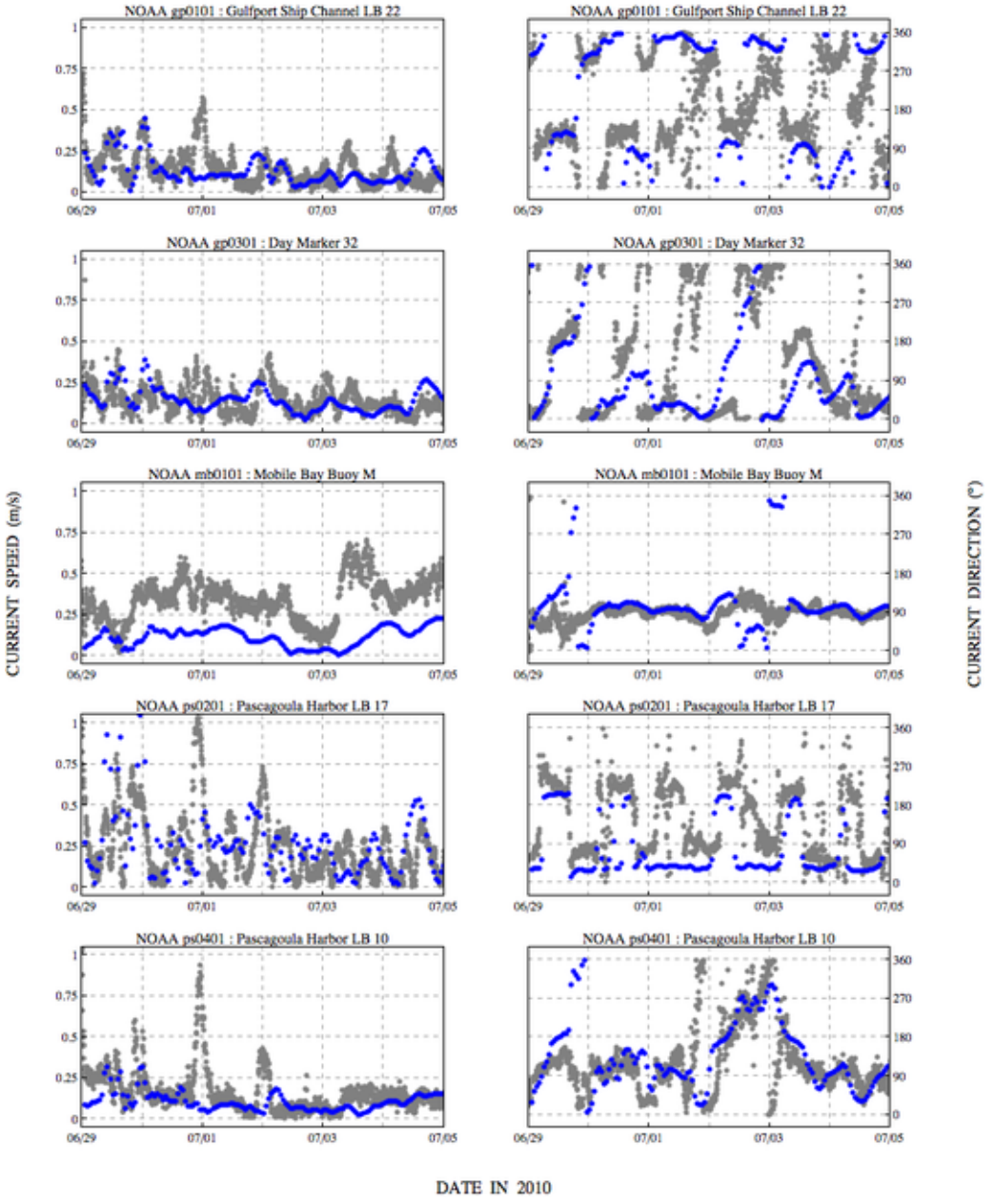

Figure 20: Current speeds (m s^{-1}) and directions (°, measured clockwise from true north) at selected NOAA stations during the Alex time period. Gray circles are measured data from NOAA, while blue circles are wind input to SWAN+ADCIRC. Station locations are shown spatially in Figure 7.

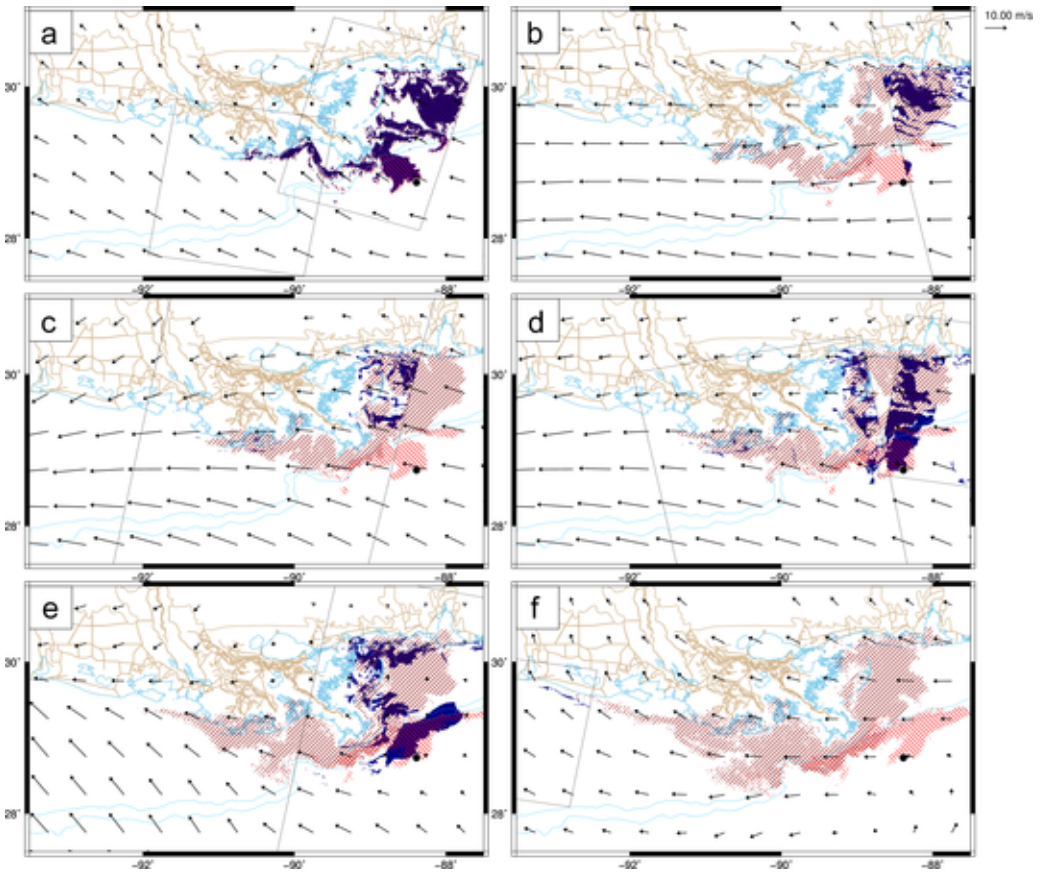

Figure 21: Comparison of observed (solid blue) and predicted (red hatched) oil extents during the Hurricane Alex time period, with forcing with currents only ($F_c = 1$ and $F_w = 0$ in Equation 1). A distinction is made between oil that started initially in deep water (light red hatching from northwest to southeast), and oil that started initially on the shelf (dark red hatching from northeast to southwest). The panels are: (a) the initial conditions on 2010/06/29/0044UTC, (b) conditions after 23hr at 2010/06/29/2332UTC, (c) conditions after 35hr at 2010/06/30/1200UTC, (d) conditions after 47hr at 2010/07/01/0005UTC, (e) conditions after 83hr at 2010/07/02/1156UTC, and (f) conditions after 143hr at 2010/07/05/0008UTC. Vectors are wind velocities (m s^{-1}), and the platform location and the extents of the satellite imagery are also indicated.

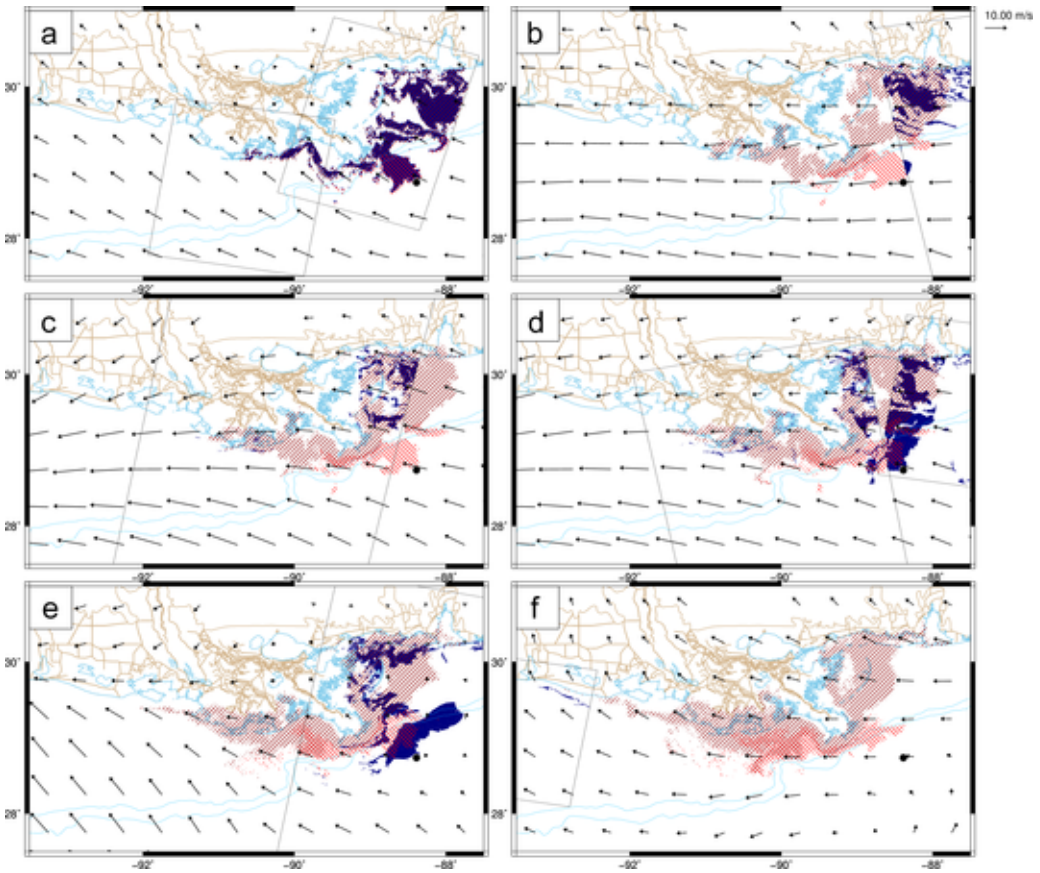

Figure 22: Comparison of observed (solid blue) and predicted (red hatched) oil extents during the Hurricane Alex time period, with forcing with currents and winds ($F_c = 1$ and $F_w = 0.01$ in Equation 1). A distinction is made between oil that started initially in deep water (light red hatching from northwest to southeast), and oil that started initially on the shelf (dark red hatching from northeast to southwest). The panels are: (a) the initial conditions on 2010/06/29/0044UTC, (b) conditions after 23hr at 2010/06/29/2332UTC, (c) conditions after 35hr at 2010/06/30/1200UTC, (d) conditions after 47hr at 2010/07/01/0005UTC, (e) conditions after 83hr at 2010/07/02/1156UTC, and (f) conditions after 143hr at 2010/07/05/0008UTC. Vectors are wind velocities (m s^{-1}), and the platform location and the extents of the satellite imagery are also indicated.

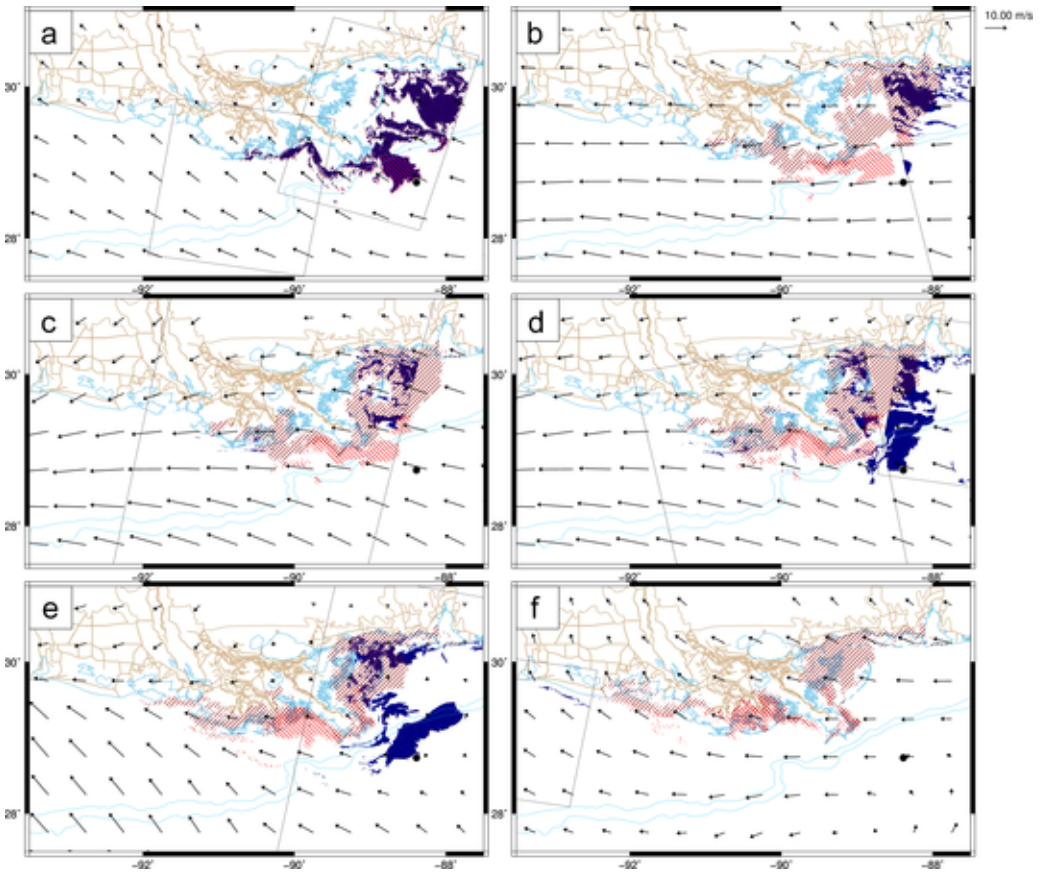

Figure 23: Comparison of observed (solid blue) and predicted (red hatched) oil extents during the Hurricane Alex time period, with forcing with currents and winds ($F_c = 1$ and $F_w = 0.03$ in Equation 1). A distinction is made between oil that started initially in deep water (light red hatching from northwest to southeast), and oil that started initially on the shelf (dark red hatching from northeast to southwest). The panels are: (a) the initial conditions on 2010/06/29/0044UTC, (b) conditions after 23hr at 2010/06/29/2332UTC, (c) conditions after 35hr at 2010/06/30/1200UTC, (d) conditions after 47hr at 2010/07/01/0005UTC, (e) conditions after 83hr at 2010/07/02/1156UTC, and (f) conditions after 143hr at 2010/07/05/0008UTC. Vectors are wind velocities (m s^{-1}), and the platform location and the extents of the satellite imagery are also indicated.

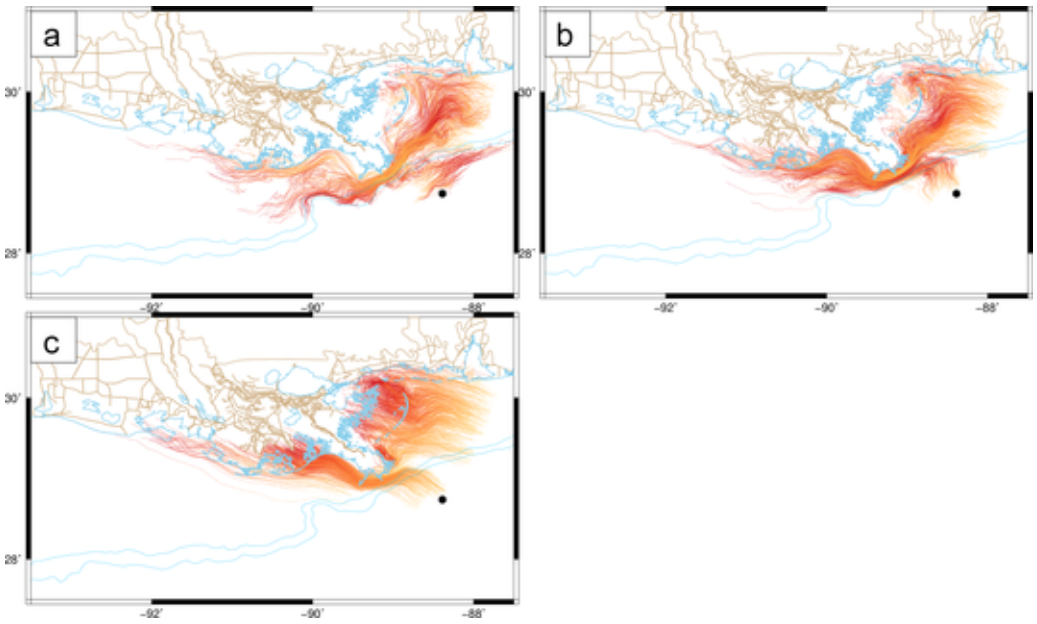

Figure 24: Sampled predicted particle locations in time during Alex, with forcings from: (a) currents only, (b) currents and 1-percent winds, and (c) currents and 3-percent winds. Particle movement is shown with the trajectories moving from orange to red. Blue lines indicate the 0m, 100m and 200m bathymetric contours, while brown lines indicate the SL16 internal road/levee boundaries.

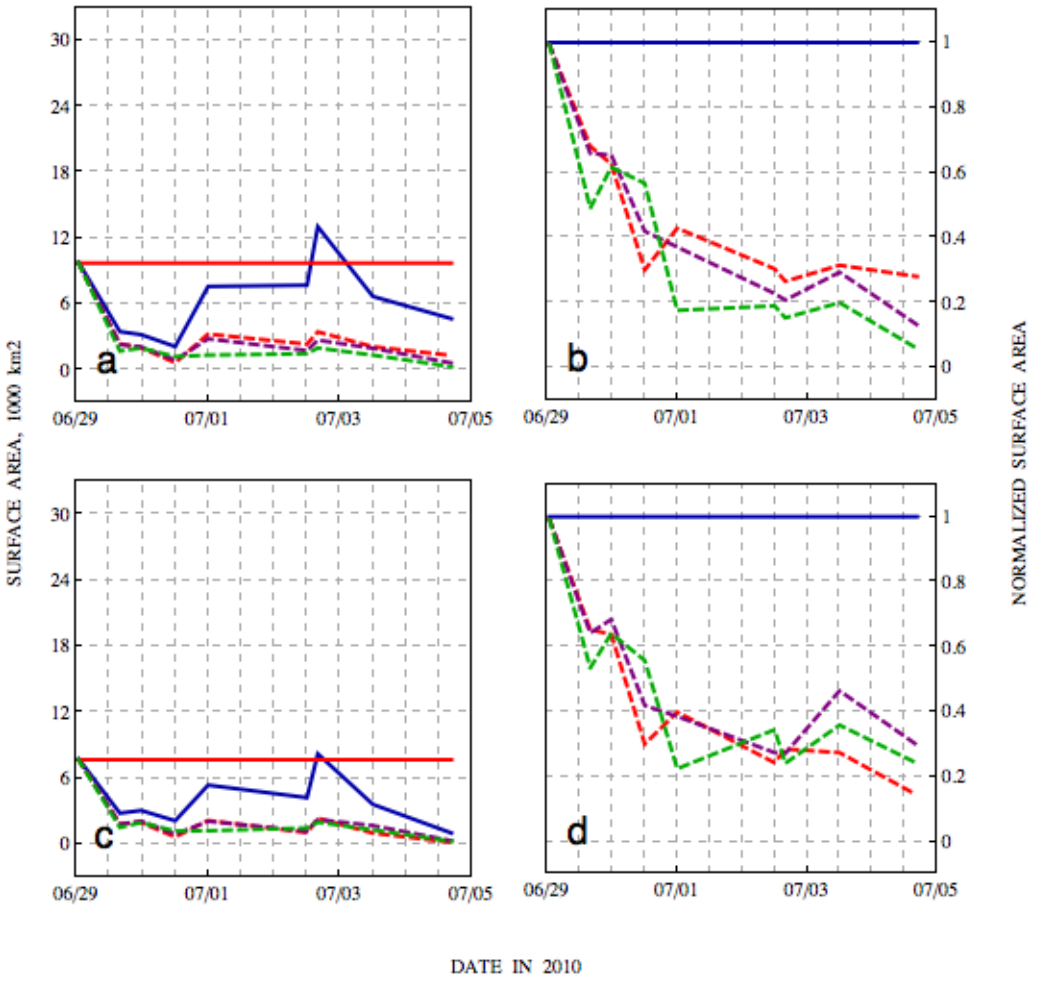

Figure 25: Total surface areas of the observed oil spill (solid blue) and particle tracers (solid red) during Alex, as well as the overlapping areas from the currents/winds scenarios: currents only (dashed red), currents and 1-percent winds (dashed purple), and currents and 3-percent winds (dashed green). The panels are: (a) areas in 1000km^2 and (b) normalized areas for oil everywhere, as well as (c) areas in 1000km^2 and (d) normalized areas for oil only on the continental shelf. In panels (b) and (d), areas are normalized with respect to the observations.

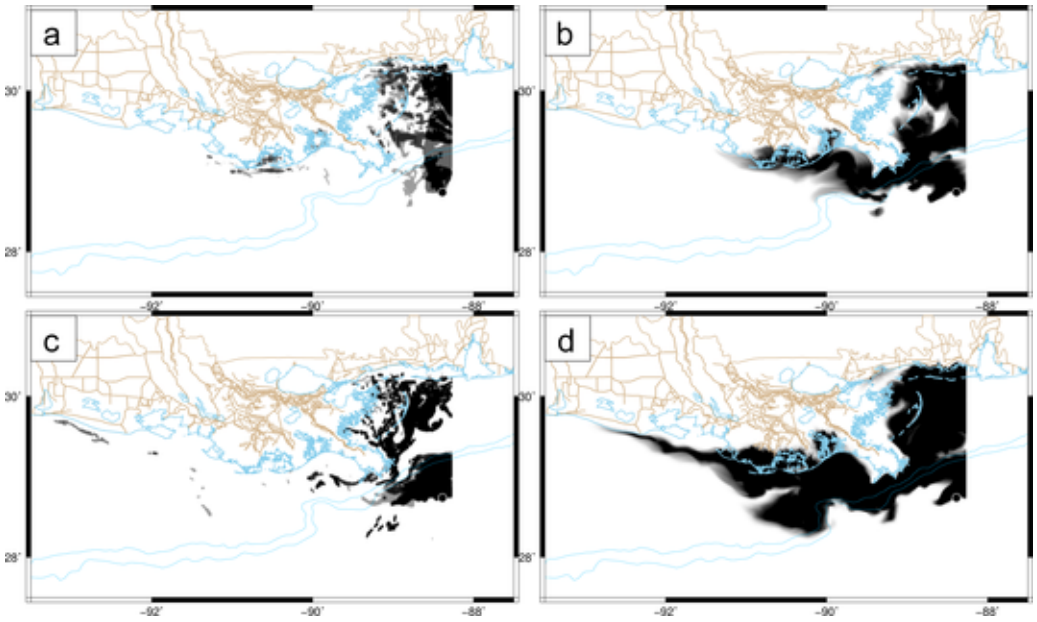

Figure 26: Samples of aggregation of satellite imagery and predicted particle locations (with currents only) during Alex. Regions without oil are shown in white, while regions with oil are shown in shades of gray and black. Oil east of Mobile Bay is disregarded for this analysis, because it was not present in the initial conditions. The panels are: (a) observations and (b) predictions aggregated over a 24hr window around 2010/06/29/2322 UTC, as well as (c) observations and (d) predictions aggregated over a 24hr window around 2010/07/04/1216 UTC. Blue lines indicate the 0m, 100m and 200m bathymetric contours, while brown lines indicate the SL16 internal road/levee boundaries. The platform location is also indicated.

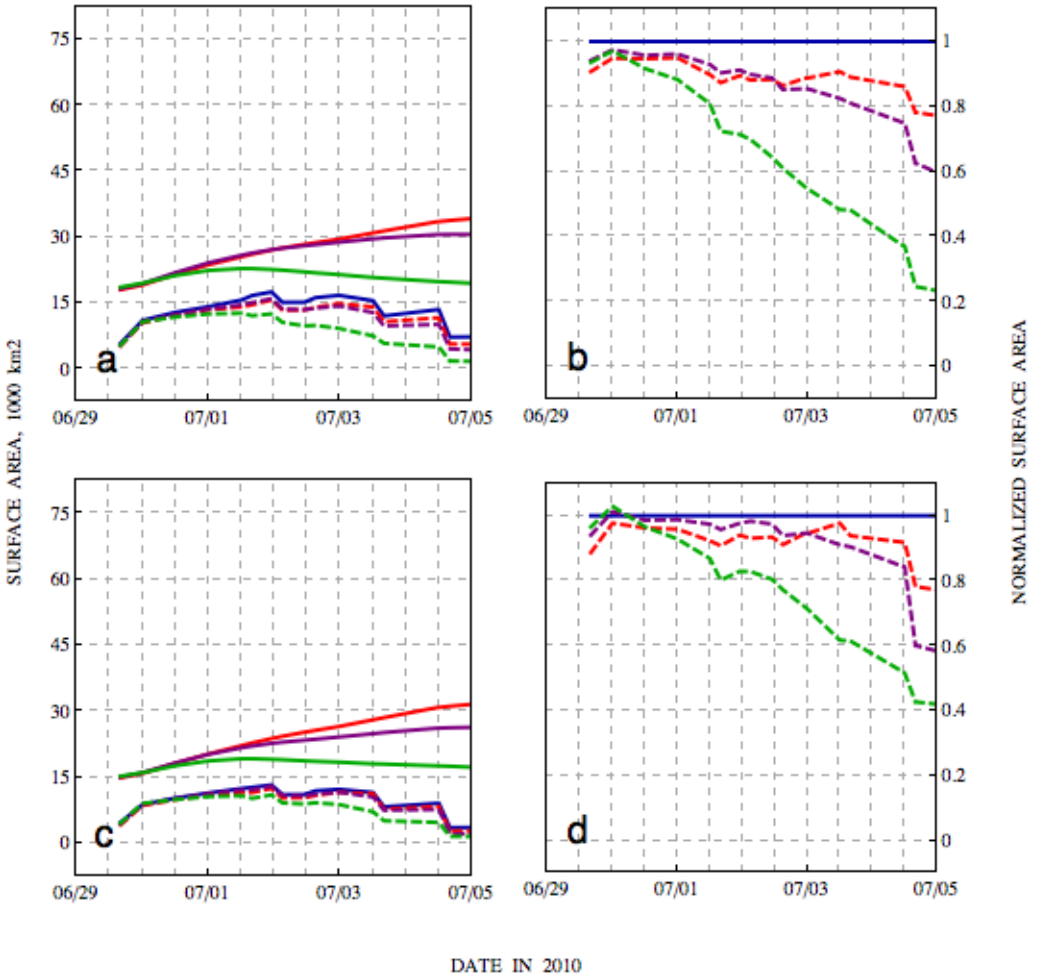

Figure 27: Total surface areas, using the larger aggregation window, of the observed oil spill (solid blue) and particle tracers (solid red, purple and green) during Alex, as well as the overlapping areas from the currents/winds scenarios: currents only (dashed red), currents and 1-percent winds (dashed purple), and currents and 3-percent winds (dashed green). The panels are: (a) areas in 1000km^2 and (b) normalized areas for oil everywhere, as well as (c) areas in 1000km^2 and (d) normalized areas for oil only on the continental shelf. In panels (b) and (d), areas are normalized with respect to the observations.

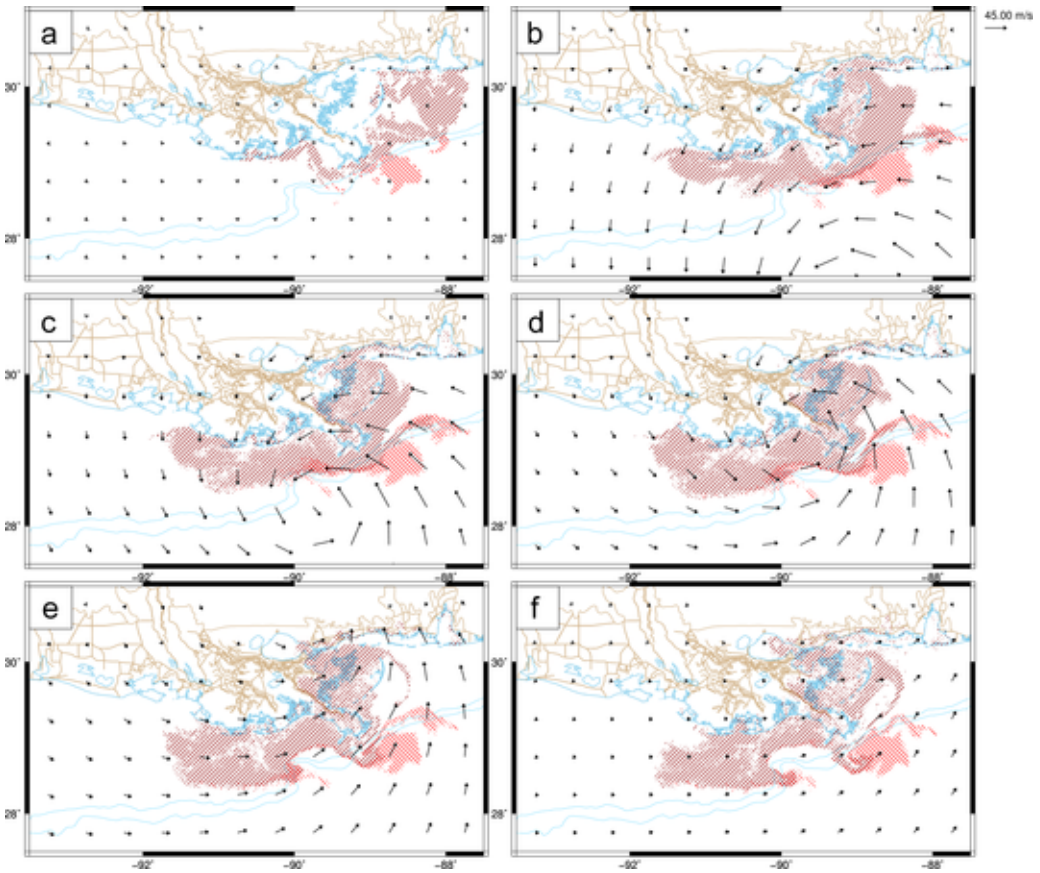

Figure 28: Hypothetical (red hatched) oil extents during Hurricane Katrina (2005), with initial conditions to match the observed oil extents on 2010/06/29/0044UTC, and with forcing with currents only ($F_c = 1$ and $F_w = 0$ in Equation 1). A distinction is made between oil that started initially in deep water (light red hatching from northwest to southeast), and oil that started initially on the shelf (dark red hatching from northeast to southwest). The panels are: (a) the initial conditions applied to 2005/08/25/0100UTC, (b) conditions after 95hr at 2005/08/29/0000UTC, (c) conditions after 102hr at landfall on 2005/08/29/0700UTC, (d) conditions after 106hr at 2005/08/29/1100UTC, (e) conditions after 111hr at 2005/08/29/1600UTC, and (f) conditions after 119hr at 2005/08/30/0000UTC. Vectors are wind velocities (m s^{-1}).

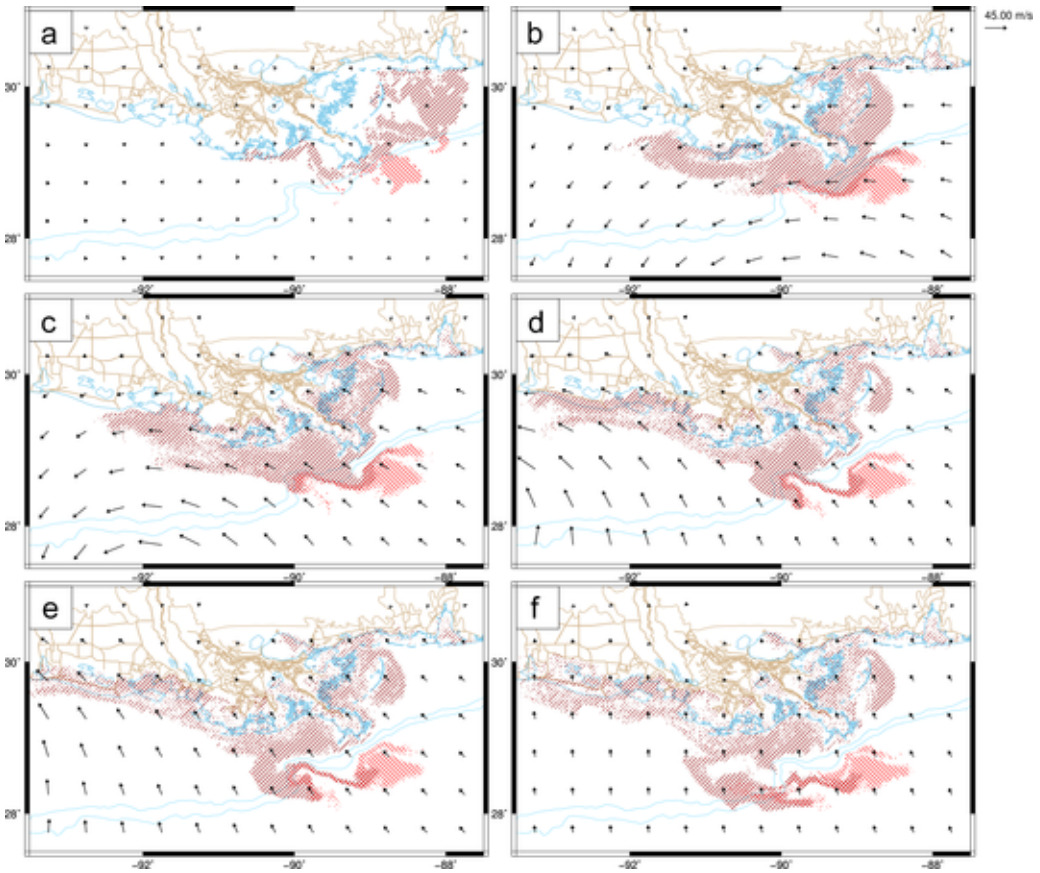

Figure 29: Hypothetical (red hatched) oil extents during Hurricane Ike (2008), with initial conditions to match the observed oil extents on 2010/06/29/0044UTC, and with forcing with currents only ($F_c = 1$ and $F_w = 0$ in Equation 1). A distinction is made between oil that started initially in deep water (light red hatching from northwest to southeast), and oil that started initially on the shelf (dark red hatching from northeast to southwest). The panels are: (a) the initial conditions applied to 2008/09/05/1300UTC, (b) conditions after 155hr at 2008/09/12/0000UTC, (c) conditions after 167hr at landfall on 2008/09/12/1200UTC, (d) conditions after 179hr at 2008/09/13/0000UTC, (e) conditions after 186hr at 2008/09/13/0700UTC, and (f) conditions after 198hr at 2008/09/13/1900UTC. Vectors are wind velocities (m s^{-1}).